Deep Resources Engineering 1 (2024) 100111

Contents lists available at ScienceDirect

Deep Resources Engineering

journal homepage: www.keaipublishing.com/en/journals/deepre/

Full Length Article

A microscopic approach to brittle creep and time-dependent fracturing of rocks based on stress corrosion model

Tao Xu [a,*], Zhen Heng [a], Ben Liu [a], Michael J. Heap [b,c], P.L.P. Wasantha [d], Zhiguo Li [a]

[a] Center for Rock Instability and Seismicity Research, Northeastern University, Shenyang 110819, China
[b] Université de Strasbourg, CNRS, Institut Terre et Environnement de Strasbourg, UMR 7063, 5 rue Descartes, Strasbourg F-67084, France
[c] Institut Universitaire de France (IUF), Paris, France
[d] College of Sport, Health and Engineering, Victoria University, Melbourne, Australia

ARTICLE INFO

Keywords:
Time-dependent cracking
Creep
Damage
Brittle rocks
Micromechanical modeling

ABSTRACT

A brittle creep and time-dependent fracturing process model of rock is established by incorporating the stress corrosion model into discrete element method to analyze the creep behavior and microcrack evolution in brittle rocks at a micro-scale level. Experimental validation of the model is performed, followed by numerical simulations to investigate the creep properties and microcrack evolution in rocks under single-stage loading, multi-stage loading, and confining pressure, at various constant stress levels. The results demonstrate that as the stress level increases in single-stage creep simulations, the time-to-failure progressively decreases. The growth of microcracks during uniaxial creep occurs in three stages, with tensile microcracks being predominant and the spatial distribution of microcracks becoming more dispersed at higher stress levels. In multi-stage loading-unloading simulations, microcracks continue to form during the unloading stage, indicating cumulative damage resulting from increased axial stress. Additionally, the creep behaviour of rocks under confining pressure is not solely determined by the magnitude of the confining pressure, but is also influenced by the magnitude of the axial stress. The findings contribute to a better understanding of rock deformation and failure processes under different loading conditions, and they can be valuable for applications in rock mechanics and rock engineering.

1. Introduction

Brittle creep in rock is a phenomenon characterized by the progressive increase in the strain of rocks over time when subjected to a constant external load [1,2]. When subjected to a constant external load, the creep strain rate first decreases to a minimum, before accelerating as the specimen approaches macroscopic failure [3]. Brittle creep has been observed in many different rock types, including granite[4,5], sandstone [6–9], limestone [10,11], and basalt [12]. Brittle creep is considered to be promoted by subcritical crack growth [13]. With the exception of limestone, for which pressure solution is considered important [10], stress corrosion microcracking is considered to be the main mechanism responsible for brittle creep in rocks [2,13]. The efficiency of stress corrosion microcracking, and therefore the rate of brittle creep in rock, depends on environmental factors such as temperature, pressure, and the pH of the pore fluid [2,13,14]. The understanding of brittle creep in rock holds significant importance for various aspects of rock engineering, such as slope stability [15,16], tunnel and underground construction [17,18], mine design, rock mass control, seismology, and geological radioactive waste disposal [19] and geophysical phenomena in the Earth's crust [6,20–22]. Consequently, extensive research on brittle creep in rock is of utmost importance and practical value in the field of rock engineering.

Currently, theoretical models and laboratory experiments are widely employed to investigate rock creep, leading to substantial advancements in the field. In terms of theoretical models, classic combined component models that combine multiple components, such as dashpots, springs, and sliders, to simulate the behavior of a complex system or mechanism, have gained a wide application. Each component represents a specific aspect of the system and contributes to its overall response in classic combined component models. For instance, Ma et al. [23] explored the creep behavior of rock salt using the Burger's model and determined the optimal parameters of the model through probabilistic analysis. One potential limitation of the combined component model is the complexity and challenge of accurately determining and calibrating the parameters and interactions of the individual components, which can affect the overall accuracy and reliability of the model's predictions. Considering

* Corresponding author.
E-mail address: xutao@mail.neu.edu.cn (T. Xu).

https://doi.org/10.1016/j.deepre.2024.100111
Received 21 June 2024; Received in revised form 13 August 2024; Accepted 20 August 2024
Available online 31 August 2024

Nomenclatures

A	the area of the parallel-bond cross-section
$\overline{D}$	the diameter of parallel bond
E^*	the apparent activation energy
E^+	the stress-free activation energy
F	the force
$\overline{F}^n$	the normal-directed force component
$\overline{F}^s$	the shear-directed force component
I	the moment of inertia of the parallel-bond cross-section
J	the polar moment of inertia of the parallel-bond cross-section
$\overline{k}^n$	the normal stiffness of parallel bond per unit area
$\overline{k}^s$	the shear stiffness of parallel bond per unit area
k_{ratio}	the ratio of normal to shear stiffness
M	the bending moment
$\overline{M}^n$	the normal-directed moment
$\overline{M}^s$	the shear-directed moment
n	the normal direction and
s	the tangential direction
R	the universal gas constant
$\overline{R}$	the radius of the cemented zone
R^A	the radius of the bonded particle A
R^B	the radius of the bonded particle B
t	the thickness of the contact bond
t_f	the creep failure time
T	the absolute temperature
ΔU^n	the axial-directed relative displacement between the two bonded particles
ΔU^s	the shear-directed relative displacement between the two bonded particles
$\Delta\theta^n$	the axial-directed relative rotation between the two bonded particles
$\Delta\theta^s$	the shear-directed relative rotation between the two bonded particles
$\overline{\sigma}_a$	the micro-activation stress
$\overline{\sigma}_c$	the tensile strength of the parallel bond
$\overline{\tau}_c$	the shear strength of the parallel bond
V_0	an experimental constant
v^+	the activation volume
α	the constant of proportionality between the corrosion rate and the reaction rate
β_1	the rate constant with units of velocity
β_2	the dimensionless constant
σ	the crack-tip stress
γ	the interfacial surface energy between the glass and the reaction products
ρ	the radius of curvature of the crack tip
v_M	the molar volume

the influence of initial damage state, Hou et al. [24] proposed a novel nonlinear creep damage model for rocks, facilitating the prediction of creep behavior in sandstone under various initial damage conditions. Additionally, Liu et al. [25] introduced a nonlinear creep damage model that incorporated the effect of water, and its accuracy was validated through triaxial creep tests conducted on both saturated and dry sandstone samples. Brantut et al. [26] incorporated subcritical crack growth into the micromechanical wing-crack model of Ashby and Sammis [27] and found that the model results compare well with data from experiments performed on granite, sandstone, and basalt. Nishihara [28] proposed a model for predicting creep-time relations of a material under various constant stresses from a strain-time relation under a certain stress-rate, which is now widely known as Nishihara model. These models can only provide the temporal evolution of strain and damage during creep, but it's challenging to model its spatial distribution, localization before failure, or the size distribution of damage events.

In terms of laboratory tests, creep tests on rock in laboratory offer the advantage of providing controlled conditions to study the time-dependent deformation behavior of rocks, allowing for the characterization of creep properties and the development of predictive models for long-term geological and engineering applications. Some studies (e.g., [29–31]) show that the creep of rock observed in laboratory tests exhibits three distinct stages: decelerating creep, steady-state creep, and accelerating creep. However, Brantut et al. [3] later showed that there is no steady-state creep phase. They showed that the strain rate first decelerates to a minimum before accelerating as the specimen approaches macroscopic failure. In general, the experimentally-derived relationships between differential stress and creep strain rate can be adequately fitted to either a power law [32–35] or an exponential law [36–38]. Using a stress-stepping approach, Heap et al. [6] studied the influence of differential stress, effective pressure, and pore fluid pressure on the creep strain rate of porous sandstone. These authors found that increasing the differential stress and effective pressure increases and decreases the creep strain rate, respectively. However, increasing the pore fluid pressure (at a constant effective pressure) did not influence the creep strain rate. Heap et al. [6] showed that, for the range of strain rates measurable in the laboratory, the relationship between creep strain rate and differential stress can be well described by a power law and an exponential function.

However, rocks are often inherently heterogeneous, and can contain discontinuities as well as anisotropy due to the presence of natural microcracks and weak planes [39,40]. Consequently, problems encountered in rock mechanics often defy straightforward analytical solutions. Conversely, numerical analysis methods offer notable advantages such as low cost, high precision, and efficiency. The remarkable advancements in computer technology have significantly expanded the applicability of numerical analysis methods. These methods not only enable the simulation of complex mechanical and structural properties of rock masses, but also facilitate the analysis of diverse boundary value problems. They can simulate and calculate potential hazards in rock engineering, thereby improving the safety and stable operation of engineering projects. Consequently, numerical analysis methods are widely recognized as effective tools for addressing geotechnical engineering problems [41–43].

Different principles of numerical computation give rise to various commonly used methods, such as the finite element method (FEM), finite difference method (FDM), discrete element method (DEM), and hybrid finite-discrete element method (FDEM) [44,45]. Among these, the DEM has emerged as a crucial approach for investigating rock mechanics problems due to its capability to simulate large deformations and phenomena such as discontinuities [46–48]. For example, Chen and Konietzky [43] employed distinct element software based on subcritical crack growth theory to conduct numerical simulations of creep instability in brittle rocks. Tiedtke et al. [49] developed a novel DFN-DEM modelling approach to simulate long-term behavior of crystalline rock under effects of glacial climate conditions. Xia et al. [50] validated the effectiveness of their numerical model using creep tests and uniaxial loading tests on specimens containing pre-existing cracks. They used an improved simulation method grounded in the classical Burger's model and the parallel bonding model in Particle Flow Code (PFC). Potyondy [51] developed a parallel bonding stress corrosion model in the two-dimensional particle flow code, PFC2D, drawing on stress corrosion

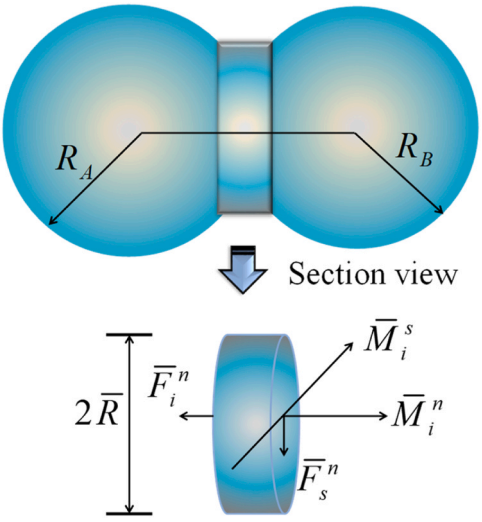

Fig. 1. The parallel bond model in particle flow code.

theory to simulate stress corrosion reactions in wet silicate rocks. In a similar manner, other studies such as [52,53] have also employed PFC2D to perform discrete element simulations focused on rock creep instability. Yang et al. [54] used a three-dimensional particle flow code, PFC-3D, based on the Burgers model to simulate rock creep processes, examining the influence of elastic coefficients, viscous coefficients, and friction factors in the Burgers model on instantaneous strength and rheological properties. Finally, Hu et al. [55] combined the equivalent crystal model with the parallel bonding stress corrosion model to investigate the impact of the non-uniform distribution of mineral grain sizes on the creep strain rate and the long-term strength of granite under uniaxial creep loading. In summary, these numerical methods offer valuable insights into rock mechanics, empowering researchers to analyze and comprehend various facets of rock behavior and deformation.

However, despite the ability of the aforementioned methods to simulate the deformation characteristics of rocks during brittle creep, most of the studies have focused on describing the apparent phenomena of creep, such as fitting creep curves and simulating failure modes. There is still a lack of in-depth understanding regarding the internal damage mechanisms and evolution of microcrack characteristics of rocks during the creep process. Therefore, this study introduces a stress corrosion model into the three-dimensional PFC3D, establishing a time-dependent deformation damage and fracture model of rock based on the discrete element method. Using this model, numerical simulations are conducted to investigate creep damage and failure processes of rocks under single-stage creep loading, multistage creep loading, and under confining pressure, at different stress levels. The aim is to reveal the creep instability mechanism from a microscopic perspective and provide some references and theoretical guidance for issues related to the long-term stability of rock engineering projects.

2. Implementation of stress corrosion model

2.1. Principles of PFC3D

A 3-dimensional particle flow code (PFC3D) model consists of rigid balls that can overlap at contact points using a soft contact approach. The calculation cycle in PFC employs a time-stepping algorithm, where Newton's law of motion is applied repeatedly to each particle, and a force-displacement law is applied to each contact. This allows the interaction between particles and their motion to be modeled.

PFC incorporates two types of bonded models: the contact bonded model and the parallel bonded model [21,56]. A contact bond can be envisioned as a pair of elastic springs with constant normal and shear stiffness acting at the contact point. The contact bonded model is capable of simultaneously carrying forces, but not moments. On the other hand, the parallel bonded model simulates the mechanical behavior of a finite-sized cement-like material deposited between two contacting pieces. This material acts in parallel with the linear component and establishes an elastic interaction between the pieces. The presence of a parallel bond does not exclude the possibility of slip, and it can transmit both force and moment between the pieces. Conceptually, a parallel bond can be understood as a collection of elastic springs with constant normal and shear stiffness that are uniformly distributed over a rectangular cross-section in 2D or a circular cross-section in 3D. These springs are located on the contact plane and centered at the contact point. They work in parallel with the springs of the linear component to provide the desired mechanical behavior. The bonded-particle model (BPM) is commonly used to simulate rocks or rock-like materials [51]. A schematic diagram of the parallel bonded model is shown in Fig. 1, where $\overline{R}$ is the radius of the cemented zone. $\overline{R}$ can be defined as $\overline{R} = \overline{\lambda}\min(R^A, R^B)$, where $\overline{\lambda}$ is the bond radius multiplier, R^A and R^B are the radii of the bonded particles, F is the force, and M is the bending moment. The superscript represents the direction, where n is the normal direction and s is the tangential direction.

The relative motion between two contact particles leads to an increase in contact forces and moments due to the contact stiffness, following Newton's law of motion. The increments in elastic force and moment carried by the parallel bond can be calculated as follows:

$$\begin{cases} \Delta\overline{F}^n = \overline{k}^n A \Delta U^n \\ \Delta\overline{F}^s = -\overline{k}^s A \Delta U^s \\ \Delta\overline{M}^n = -\overline{k}^s J \Delta\theta^n \\ \Delta\overline{M}^s = -\overline{k}^n I \Delta\theta^s \end{cases} \tag{1}$$

where $\overline{F}^n, \overline{F}^s, \overline{M}^n$, and $\overline{M}^s$ denote the normal- and shear-directed forces and moments, respectively, and $\overline{k}^n$ and $\overline{k}^s$ are the normal and shear stiffness of parallel bond per unit area, respectively. ΔU^n and ΔU^s are the axial and shear-directed relative displacements between the two bonded particles, respectively, and $\Delta\theta^n$ and $\Delta\theta^s$ are the axial and shear-directed relative rotations between the two bonded particles, respectively. A, I, and J are the area, moment of inertia, and polar moment of inertia of the parallel-bond cross-section, respectively. We have:

$$A = \begin{cases} 2\overline{R}t, & 2D \quad (t=1) \\ \pi\overline{R}^2, & 3D \end{cases}, \quad I = \begin{cases} \frac{2}{3}t\overline{R}^3, & 2D \left(t=1\right) \\ \frac{1}{4}\pi\overline{R}^4, & 3D \end{cases}, \quad J = \begin{cases} 0, & 2D \ (t=1) \\ \frac{1}{2}\pi\overline{R}^4, & 3D \end{cases}$$

where, $\overline{R}$ is the radius of the cemented zone, and t is the thickness of the contact bond. 2D and 3D represent two-dimensional and three-dimensional conditions, respectively.

The maximum tensile and shear stresses acting on the parallel-bond periphery can be calculated from beam theory, and are given by:

$$\begin{cases} \overline{\sigma} = \dfrac{-\overline{F}_i^n}{A} + \dfrac{|\overline{M}_i^s|}{I}\overline{R} \\ \overline{\tau} = \dfrac{\overline{F}_i^s}{A} + \dfrac{|\overline{M}_i^n|}{J}\overline{R} \end{cases} \tag{2}$$

where, $\overline{\sigma}_c$ and $\overline{\tau}_c$ are the tension and shear strength of the parallel bond, respectively. The parallel bond will break if either $\overline{\sigma}^{\max} > \overline{\sigma}_c$ or $\overline{\tau}^{\max} > \overline{\tau}_c$.

In our study, we assume that each bond breakage in the modeled rock corresponds to a microcrack. When the shear strength of a bond is exceeded, the resulting crack is considered to be a shear crack. On the other hand, if the tensile stress acting on a bond exceeds its tensile strength, the resulting crack is considered to be a tensile crack. It is important to note that the representation of tensile and shear cracks in our study is a simplified approach to simulate the fracture process in

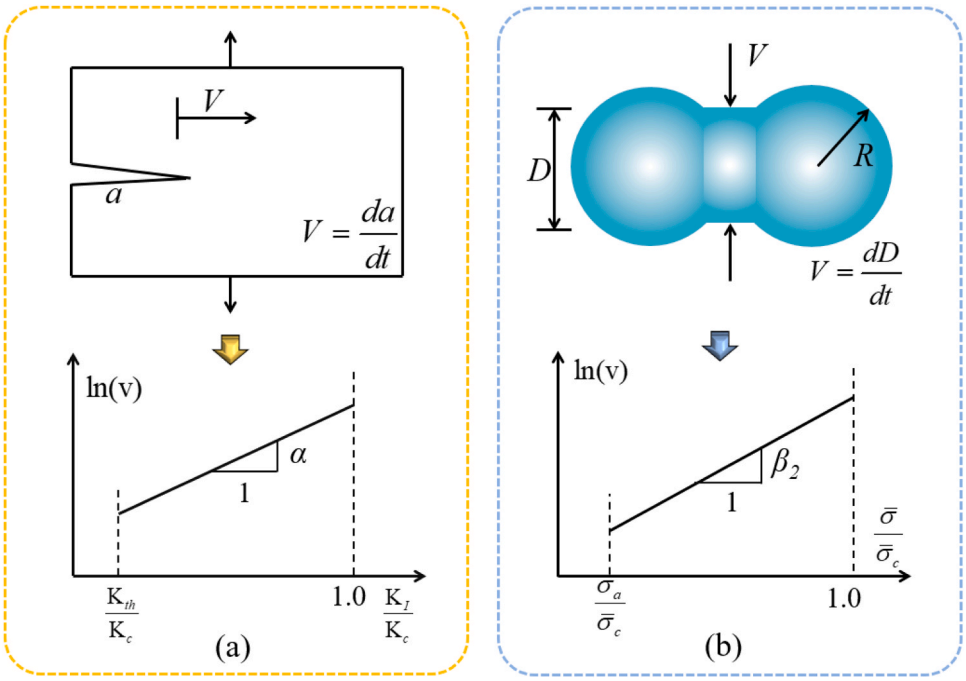

Fig. 2. Damage-rate relations for (a) LEFM and (b) PSC models.

rock. The cracks discussed here do not fully capture the complexity and intricacies of real fractures that occur in natural rock formations [57].

2.2. Description of stress corrosion model

The BPM is a representation of rock at the grain scale, where a dense packing of non-uniform-sized circular or spherical particles is used. These particles are bonded together at their contact points, and their mechanical behavior is simulated using the distinct element method. Within the BPM, the explicit representation of damage is incorporated through the presence of broken bonds, which are referred to as microcracks. These microcracks may form when loads are applied to the rock model. By tracking the state of the bonds and identifying those that are broken, the BPM can capture the development and propagation of microcracks, thus simulating the progressive damage and failure of the rock material under loading conditions.

In order to simulate time-dependent damage in rock, it is important to account for stress corrosion reactions that occur at strained defects within the rock. These defects are commonly idealized as Linear Elastic Fracture Mechanics (LEFM) cracks, where the appropriate driving force for crack growth is represented by the stress intensity factor K_I [58]. However, in the case of the parallel bonded model, K_I does not accurately characterize the stress field at the tip of an isolated microcrack. It only becomes applicable when a sufficient number of these microcracks have coalesced into a macroscopic fracture. Under compressive loading, the BPM exhibits distributed bond breakages that precede the formation of one or more shear-like faults, which corresponds to failure in rock deformation tests, including creep tests. In long-term loading scenarios, the system spends a significant amount of time in a state of distributed damage.

Therefore, it is necessary to develop a damage mechanism that does not rely upon the presence of LEFM cracks. By comparing it with the crack propagation process in fracture mechanics, Potyondy [51] proposed that the reduction in inter-particle bonding strength in the BPM can be considered as creep damage, while the fracture between contacts can be regarded as microcracks generated during the creep process due to damage. Based on this, Potyondy [51] introduced the parallel-bonded stress corrosion (PSC) model. The main concept of the PSC model is to simulate the time-dependent damage of rocks by weakening the contact strength between particles. The contact strength between particles is directly proportional to the contact radius, thus, reducing the contact radius can effectively decrease the contact strength. The proposed mechanism instead relies upon the existence of micro-tensions throughout the BPM, even in the absence of microcracks. These micro-tensions act as the driving forces for damage production. By considering these micro-tensions, the PSC model can capture the gradual accumulation of damage over time without explicitly relying on the formation of LEFM cracks. This approach allows for a more accurate representation of time-dependent damage in the BPM.

In developing a damage mechanism for the BPM, it would be ideal to establish a direct mapping between the physical system and the model system. However, deriving the form of the damage-rate law directly from reaction-rate theory is not feasible in this case. This is because the stress at the reaction site in the BPM is only equal to the tensile stress in the model if the particle size is comparable to atomic spacing. In reality, the particle sizes in the rock models used in BPM are significantly larger. Instead, the form of the damage-rate law in the BPM arises from considerations of reaction-rate theory and an analogy between the physical system and the model system. This analogy is represented in Fig. 2. The damage-rate law is determined based on these considerations, as it is the best approach given that the BPM can only resolve stresses down to the particle scale. Thus, the PSC model captures the effect of micro-tensions activating a damage process, even though direct mapping to reaction-rate theory is not possible due to the differences in scale between the BPM and the physical system.

The static fatigue theory of Hillig and Charles [59] applied to glass provides a rate equation to describe crack growth behavior:

$$V = V_0 \exp\left(\frac{-E^* + v^+\sigma}{RT}\right), \quad E^* = E^+ + v_M\gamma/\rho \tag{3}$$

where, V_0 is an experimental constant, E^* is the apparent activation energy, v^+ is the activation volume, σ is the crack-tip stress, R is the universal gas constant, and T is the absolute temperature. The apparent activation energy contains the following terms: $E^+$is the stress-free activation energy, $v_M$is the molar volume of the glass, γ is the interfacial surface energy between the glass and the reaction products, and ρ is

the radius of curvature of the crack tip.

Eq. (3) assumes that the crack velocity is proportional to the reaction rate and states that an energetically favored reaction will progress at a rate determined by the rate of successful attempts to overcome an energy barrier represented by the activation energy. In addition, if the reaction site (in this case, the material at the crack tip) is stressed, the effective energy barrier is reduced by the amount$v^{+}\sigma$.

Assuming that the time-dependent behavior of silicate rock in the brittle regime is controlled by stress corrosion reactions (in which water attacks the Si-O bonds of the material in regions experiencing large stress-induced volumetric expansion [60]) and that this reaction can be represented using reaction-rate theory, stress corrosion reactions serve as an appropriate basis for the damage-rate law of the PSC model.

The BPM mimics the mechanical behavior of a collection of grains joined by cement. In the following, we consider each grain as a single particle and each cement entity as a parallel bond. Eq. (3) is introduced into the BPM by making the following assumptions:

(a) Stress corrosion reactions only affect the cement; they do not affect the grains. Therefore, each parallel bond is a potential reaction site.
(b) Stress corrosion reactions occur at the bond surface and remove bond material at a uniform rate that is proportional to the crack velocity in Eq. (3), which is, in turn, proportional to the reaction rate. The rate of material removed is called the corrosion rate. We can envision the removal process as a uniform erosion of bond material along its periphery.
(c) The corrosion rate is dependent on the stress at the reaction boundary.
(d) Corrosion only occurs when the stress is tensile and above some threshold level.

We express the corrosion rate as the rate at which the parallel-bond diameter decreases by assumptions (a) and (b):

$$\frac{d\overline{D}}{dt} = -\left(\alpha V_0 e^{-E^*/RT}\right) e^{v^+/RT} \tag{4}$$

where, α is the constant of proportionality between the corrosion rate and the reaction rate. The reaction-site stress is taken as $\overline{\sigma}$, the maximum tensile stress acting on the parallel-bond periphery (assumption (c) above), and the threshold stress below which the stress corrosion reaction ceases (assumption (d) above) is taken as $\overline{\sigma}_a$. Therefore, Eq. (4) can be expressed as:

$$\frac{d\overline{D}}{dt} = \begin{cases} 0, & \overline{\sigma} < \overline{\sigma}_a \\ -\beta_1 e^{\beta_2\left(\frac{\overline{\sigma}}{\overline{\sigma}_c}\right)}, & \overline{\sigma}_a \le \overline{\sigma} < \overline{\sigma}_c - \infty, \quad \overline{\sigma} \ge \overline{\sigma}_c \end{cases} \tag{5}$$

where, $\overline{\sigma}$ has been normalized by the parallel-bond tensile strength, $\overline{\sigma}_c$. The damage-rate law provides the rate at which the diameter,$\overline{D}$, of each parallel bond decreases. As damage proceeds, the effective bond strength decreases, which allows for a macroscopic load redistribution to occur throughout the material. The variables are the maximum tensile stress acting on the parallel-bond periphery ($\overline{\sigma}$) and the elapsed time since bond formation (t). The parameters are the one rate constants (β_1) with units of velocity, and the dimensionless constant (β_2), the micro-activation stress ($\overline{\sigma}_a$), and the parallel-bond tensile strength ($\overline{\sigma}_c$) [61]. In the present model, In the present model, we focus on the damage/microcracking evolution and failure processes during the time-dependent deformation of rock under creep loading and confining pressure conditions. Additionally, the generalized effective stress law could be introduced into the model to conduct uniaxial compressive or constant loading simulations of the rock [61].

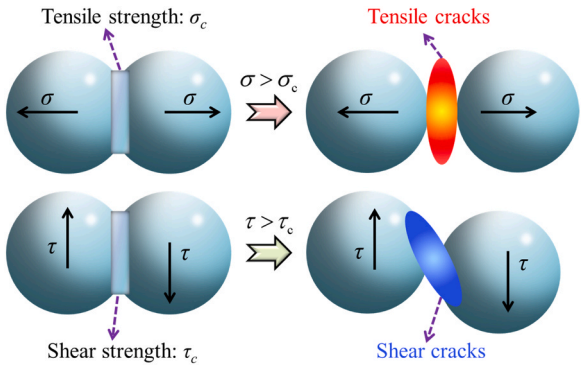

Fig. 3. The characterization of microcracking in PFC showing the formation of tensile and shear cracks.

Table 1
Parameter settings for the sensitivity analysis of the PSC model.

Scheme number	$\overline{\sigma}_a$/MPa	$B_1\times10^{-15}$	β_2
1	10	10	15
2	10	10	18
3	10	10	21
4	10	10	24
5	10	10	27
6	10	10	30
7	10	1	21
8	10	5	21
9	10	10	21
10	10	15	21
11	10	20	21
12	10	25	21
13	1	10	21
14	5	10	21
15	10	10	21
16	15	10	21
17	20	10	21
18	25	10	21

2.3. Characterization of microcracking

The characteristic behavior of rock creep is the occurrence of internal damage within the rock due to constant external loads, resulting in a reduction in its load-bearing capacity [2]. Eventually, the rock experiences macroscopic failure once it reaches a certain strain threshold. This internal damage inevitably leads to the formation of microcracks, and the PFC can accurately elucidate the entire process of microcrack generation and the consequent failure mode from a microscopic perspective. We define that a tensile microcrack forms between particles when the normal stress between them exceeds the tensile strength limit of the parallel bonding. Similarly, when the tangential stress between particles surpasses the shear strength limit of the parallel bonding, a shear microcrack forms between the particles, as illustrated in Fig. 3.

3. Calibration and validation of stress corrosion model

3.1. Sensitivity analysis for input parameters

Eq. (5) reveals that the crack growth rate of the PSC model is influenced by key parameters, namely $\overline{\sigma}_a$,$\overline{\sigma}_c$, β_1, and β_2. Among these parameters, $\overline{\sigma}_c$ is the strength parameter of the inter-particle bonding material, which controls the static strength of the model. Meanwhile, $\overline{\sigma}_a$, β_1, and β_2 collectively determine the long-term strength of the model. To analyze the impact of these parameters on the long-term strength of the PSC model, a parameter sensitivity analysis was conducted for $\overline{\sigma}_a$, β_1, and β_2 individually. Prior to the parameter sensitivity analysis, an initial test was performed to determine the approximate range of each

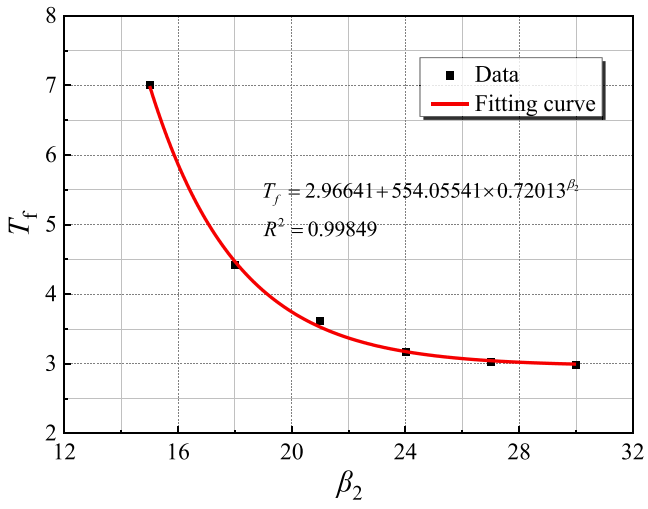

(a) The relationship between β_2 and T_f

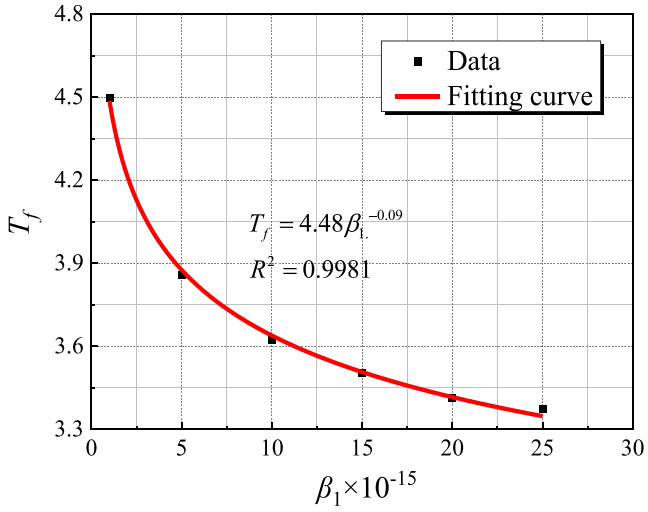

(b) The relationship between β_1 and T_f

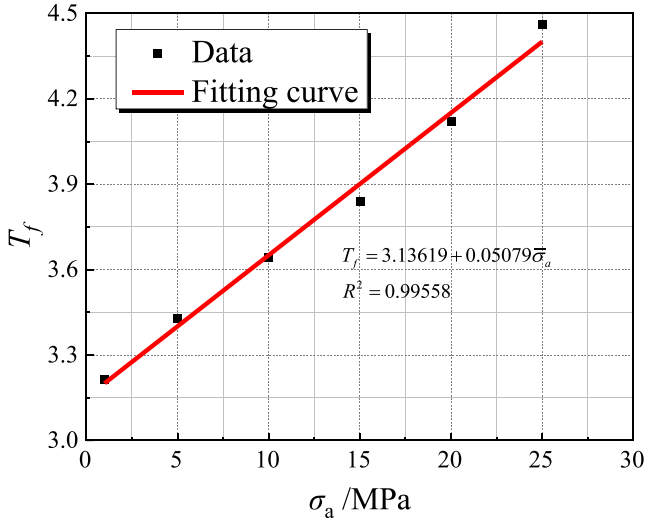

(c) The relationship between $\overline{\sigma}_a$ and T_f

Fig. 4. Results of the PSC model parameter sensitivity analysis.

parameter based on the results of laboratory uniaxial creep tests: $\overline{\sigma}_a$ ranged from 1 to 25 MPa, β_1 ranged from 1 to 25 × 10^{-15}, and β_2 ranged from 15 to 30. Subsequently, 18 sets of simulation tests were designed using these approximate parameter ranges. The constant stress for each sensitivity analysis group was set at 70 % of the stress required for the short-term failure of the specimen. During the sensitivity analysis simulations, the creep failure time (t_f) was recorded, which corresponds to the time at which the axial strain experienced a significant and sudden acceleration. A sudden acceleration in axial strain indicates macroscopic failure in a brittle creep test [2]. To facilitate the analysis, we let $T_f = \log(t_f)$. The specific parameter settings for the simulation tests are listed in Table 1.

(1) Based on the results of simulation schemes 1–6 (Table 1), it can be observed that there is an approximate exponential relationship between β_2 and T_f. As β_2 increases, T_f rapidly decreases (Fig. 4(a)). Moreover, when β_2 approaches 0, the creep failure time becomes constant.
(2) Based on the results of simulation schemes 7–12 (Table 1), it can be observed that there is an approximate power function relationship between β_1 and T_f. As β_1 increases, T_f sharply decreases (Fig. 4(b)). Additionally, when β_1 approaches 0, the model remains stable and does not experience creep failure. Conversely, when β_1 exceeds a certain threshold, the instantaneous fracture of the specimen occurs.
(3) Based on the results of simulation schemes 13–18 (Table 1), it can be observed that there is a linear relationship between $\overline{\sigma}_a$ and T_f, where increasing $\overline{\sigma}_a$ leads to a linear increase in T_f (Fig. 4(c)). This linear relationship can be attributed to the fact that increasing $\overline{\sigma}_a$ raises the threshold for exciting the PSC model among the particles. Consequently, under the same loading conditions, the number of contacts experiencing damage is reduced, making the model more resistant to failure.

Through sensitivity analysis of the PSC model parameters (Fig. 4), it is evident that β_1 and β_2 have a significant impact on the time to creep instability, while $\overline{\sigma}_a$ is positively, and linearly correlated with the instability time T_f of the model. Therefore, when determining the parameters of the PSC model, it is recommended to initially set $\overline{\sigma}_a$ to a relatively large value and gradually transition β_1 and β_2 from larger to smaller values. This approach ensures that the creep instability time of the model aligns (same order of magnitude) with the creep instability times observed in laboratory experiments. Subsequently, the value of $\overline{\sigma}_a$ can be determined.

3.2. *Calibration of input parameters for time-independent model*

The calibration of the short-term microscale parameters in the model is typically conducted using the macroscopic mechanical parameters of rock specimens in laboratory uniaxial compression tests, including the peak stress (the uniaxial compressive strength, UCS), Young's modulus, and Poisson's ratio. To achieve this calibration, a numerical model employing the PFC is established, wherein the microscale particle and contact parameters are adjusted to ensure consistency with the macroscopic mechanical properties of the laboratory rock specimens. During the laboratory tests, uniaxial compression experiments were performed on dry, cylindrical sandstone samples (50 mm in diameter and 100 mm in length). The macroscopic mechanical parameters from these experiments were: a peak axial stress of 47.27 MPa, a Young's modulus of 12.4 GPa, and a Poisson's ratio of 0.29.

In this study, the microscale mechanical parameters of the numerical model were calibrated based on the results of the laboratory uniaxial compression tests. The contact behavior between particles in the model was simulated using parallel-bonded contacts. A 3D numerical particle model with the same dimensions as the laboratory samples (i.e., 50 mm in diameter and 100 mm in length) was constructed for the calibration.

Table 2
Micro-parameters for the numerical model.

Parameters, unit	Value
Minimum particle radius d_{min}, mm	2.0
Ratio of maximum to minimum particle radius d_{max} /d_{min}	1.25
Young's modulus of particle E_c, GPa	9.0
The ratio of normal to shear stiffness k_{ratio}	2.2
The friction coefficient of particle	0.3
The friction coefficient of walls	0.15
Parallel-bond tensile strength, MPa	55
Parallel-bond shear strength, MPa	30

The calibrated, best-fit particle-level and parallel-bonded contact parameters are detailed in Table 2. The stress-strain curves obtained from the laboratory experiment and from the calibrated model are shown in Fig. 5.

During compression tests in the laboratory, micropores and microcracks that are present in natural rock specimens are initially compacted as the applied stress increases. Consequently, the stress-strain curve exhibits an initial concave shape, followed by linear elastic behavior (green curve in Fig. 5(a)). The model, however, does not contain such imperfections and, as a result, nominal values of test data are approximately obtained by shifting the curve (blue curve in Fig. 5(a)). Since Young's modulus of the rock is calculated as the slope of the stress-strain curve in the elastic stage, it is common to shift experimental curves to the left to eliminate the initial crack compaction stage, in order to better facilitate the comparison between the laboratory and numerical curves [62], as we have done in Fig. 5(a). As shown in Fig. 5(a), it can be observed that the numerically simulated curve (red curve) generally agrees well with the nominal values of the test curve (blue curve). We also note that the failure mechanism of the laboratory specimen (Fig. 5 (b)) is very similar to that of the numerical specimen (Fig. 5(c)).

In order to further validate the numerical model developed in this study, the same rock numerical model was used to simulate compression tests under different confining pressures. Stress-strain curves for simulations performed under confining pressures of 0, 5, 10, 20, 30, and 40 MPa are shown in Fig. 6. As shown in Fig. 6, peak differential stress increases as a function of increasing confining pressure, as observed in laboratory experiments performed in the brittle field [63]. We also note that the stress drop following macroscopic failure is less pronounced as confining pressure increases (Fig. 6), which is also in line with laboratory experiments performed in the brittle field [63].

By comparing the compressive strength obtained from the numerical model under different confining pressures with the results from laboratory tests, it was observed that the compressive strength of the rock exhibited a good fit with the experimental results at low confining pressures (0–20 MPa) (Fig. 7). However, at confining pressures above 20 MPa, there was an increasing discrepancy between the simulated and experimental results (Fig. 7). Nevertheless, both the experimental and simulated results showed a linear relationship between peak stress and confining pressure, following the Mohr-Coulomb criterion (Fig. 7). Therefore, the adoption of the PFC model proves effective in simulating the fundamental mechanical properties of rock.

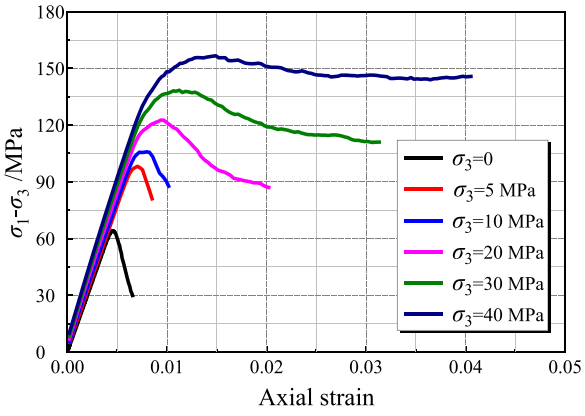

Fig. 6. The stress-strain curves for numerical simulations performed at different confining pressures.

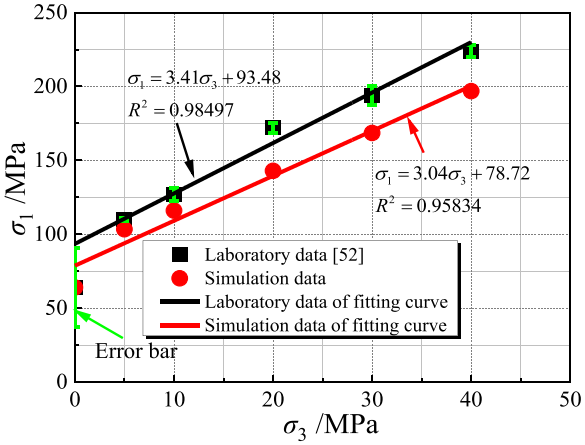

Fig. 7. The relationship between compressive strength and confining pressure for laboratory experiments [63] (in black) and numerical simulations (in red).

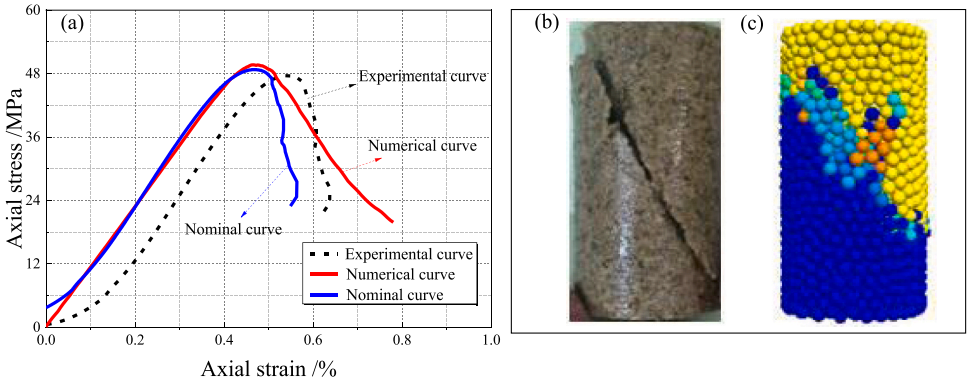

Fig. 5. Comparisons between experimental results and numerical simulations of sandstone. (a) Stress-strain curves, (b) Failure mechanism of the specimen (100 mm in length) in the laboratory test, and (c) Failure mechanism of the specimen (100 mm in length) in the numerical simulation.

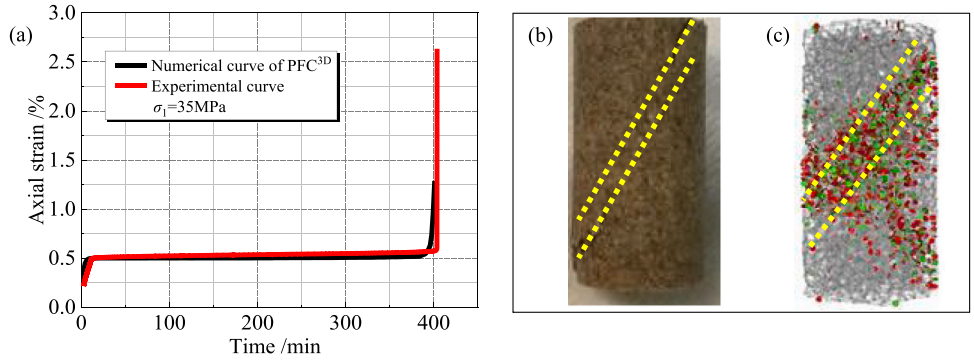

Fig. 8. Comparisons between the results of experimental uniaxial creep tests and numerical uniaxial creep simulations. (a) Creep curves for the laboratory experiment and the numerical simulation. (b) Photograph of the failed laboratory specimen. Yellow dashed lines show the position of the shear fracture. (c) Image showing the failed specimen following the numerical creep simulation. Yellow dashed lines show the position of the shear fracture. Red color represents tensile microcracks, and green color represents shear microcracks.

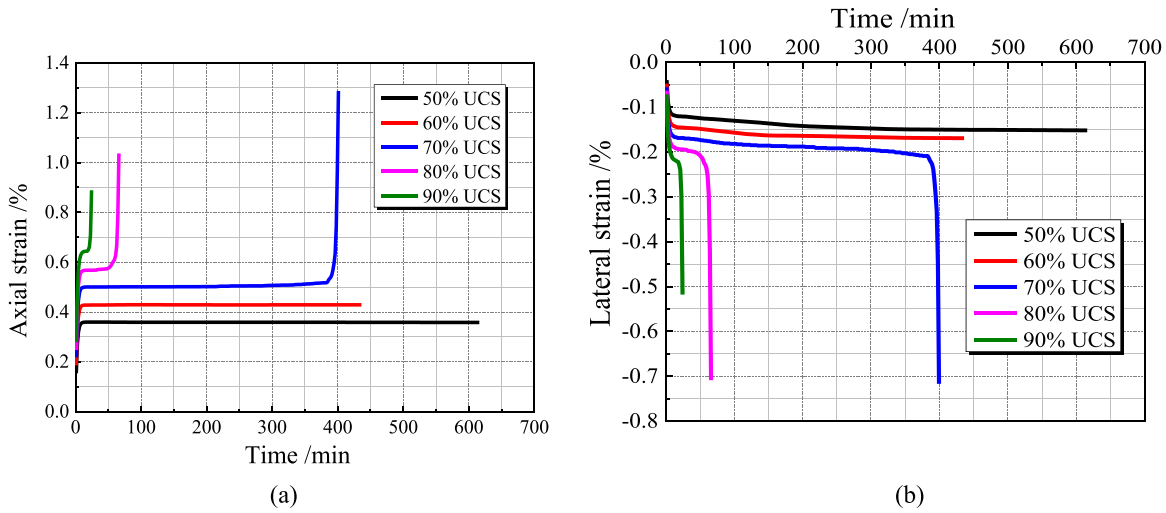

Fig. 9. Numerical (a) axial and (b) lateral strain creep curves of brittle rocks at different stress levels of 50 %, 60 %, 70 %, 80 %, and 90 % of the UCS.

3.3. *Calibration of input parameters for time-dependent model*

A PFC model that reflects the short-term (i.e., time-independent) mechanical characteristics of the rock specimens was established based on calibrated short-term microstructural parameters in the previous section. By adjusting the main parameters of the PSC model, namely β_1, β_2 and$\overline{\sigma}_a$, it is possible to calibrate the PFC model to perform numerical uniaxial creep tests (i.e., time-dependent). First, the parameters β_1, β_2 and$\overline{\sigma}_a$ must be determined. To do so, we performed numerical uniaxial creep test simulations, in which numerical rock specimens were held at a constant stress equal to 70 % of its UCS, in which we varied β_1, β_2 and$\overline{\sigma}_a$. By comparing the results of these simulations with the results from a laboratory uniaxial creep test, also held at 70 % of its UCS, we are able to determine the most appropriate values for β_1, β_2 and$\overline{\sigma}_a$. Based on this calibration, we found $\beta_1 = 8 \times 10^{-15}$, $\beta_2 =$ 18.5, and $\overline{\sigma}_a = 10$ MPa.

Fig. 8 shows the creep curves (axial strain versus time) obtained from the numerical simulation and the laboratory experiment (Fig. 8(a)), and the final creep failure mode for both the experimental rock sample (Fig. 8(b)) and the numerical simulation (Fig. 8(c)). From Fig. 8, it can be observed that the results from the numerical simulation align well with the results from the laboratory experiment. The simulation results not only effectively capture the decelerating and accelerating creep stages of the laboratory creep test, including similar values for the instantaneous elastic strain ε_e, creep strain rate $\dot{\varepsilon}_2$, and time-to-failure t_f (Fig. 8(a)), but also demonstrate the process of microcrack initiation and propagation, and their coalescence into a macroscopic shear fracture (Fig. 8(c)). Similar creep curves, characterized by a decelerating stage followed by an accelerating stage, have been previously reported for many different rock types (see review by Brantut et al. [2]).

4. Modeling of creep of brittle rock

4.1. *Conventional single-stage creep tests*

4.1.1. *Creep under different levels of loading*

To investigate the creep deformation behavior of rocks under single-stage loading conditions (i.e., “conventional” creep tests), we conducted uniaxial creep simulations on rocks at various constant stress levels (50 %, 60 %, 70 %, 80 %, and 90 % of the UCS) using the creep model described in the previous section. A series of creep curves for rocks at different stress levels were obtained, as shown in Fig. 9. At stress levels of 50 % and 60 % of the UCS, the axial strain of the model remains approximately constant: the axial creep strain rate decelerates to close to zero, indicating a long-term stability (Fig. 9(a)). On the other hand, under stress levels of 70 %, 80 %, and 90 % of the UCS, the rock exhibits both decelerating and accelerating creep, and, ultimately, macroscopic failure (indicated by the large increases in axial strain) (Fig. 9(a)). The lateral creep curves follow the same pattern as the axial creep curves, as illustrated in Fig. 9(b).

The variations of creep strain rates with time for different axial stress levels are presented in Fig. 10. According to Fig. 10, the axial creep

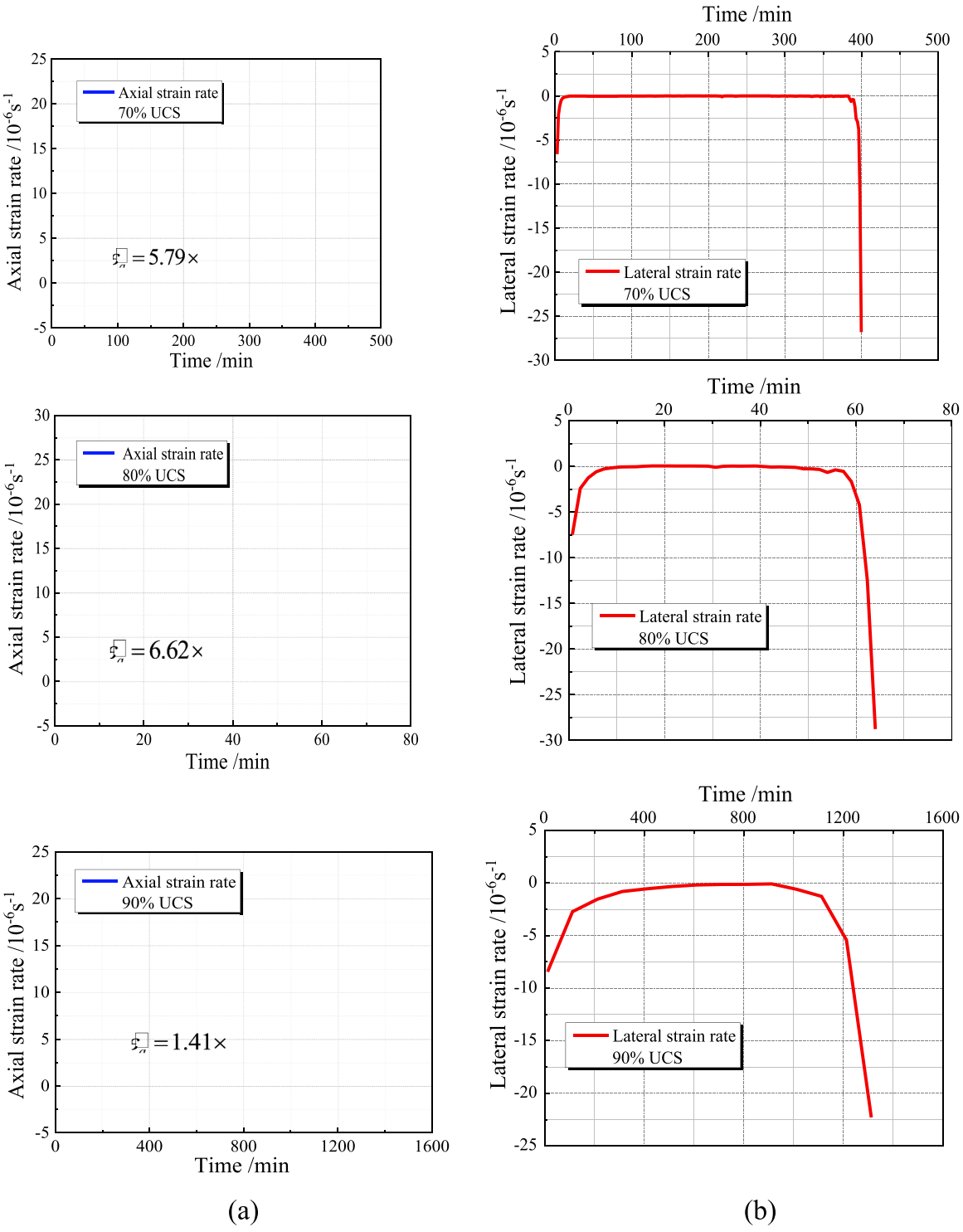

Fig. 10. The variations of creep strain rate with time for different stress levels (70 %, 80 %, and 90 % of the UCS). (a)axial creep strain rate, (b) lateral creep strain rate.

strain rates for the numerical specimens are 5.79 × 10^{-9} s^{-1} , 3.32 × 10^{-8} s^{-1} and 1.10 × 10^{-7} s^{-1}, respectively, for the stress levels of 70 %, 80 %, and 90 % of the UCS. It was found that increasing the stress by only 10 % of the UCS increases the axial creep strain rate by about an order of magnitude. Similarly, the corresponding lateral creep strain rates are 1.52 × 10^{-8} s^{-1} , 1.14 × 10^{-7} s^{-1} and 7.12 × 10^{-7} s^{-1}, respectively.

Fig. 11 illustrates the variations of the axial and lateral creep strain rates (on a logarithmic scale) of the numerical specimens as a function of initial axial stress applied. As depicted in Fig. 11, both the axial and lateral creep strain rates demonstrate a linear correlation with the stress level in semi-log plots. These numerical simulation results align with previous experimental observations [2,6,64]. It is worth noting that even minor alterations in stress levels can result in significant variations

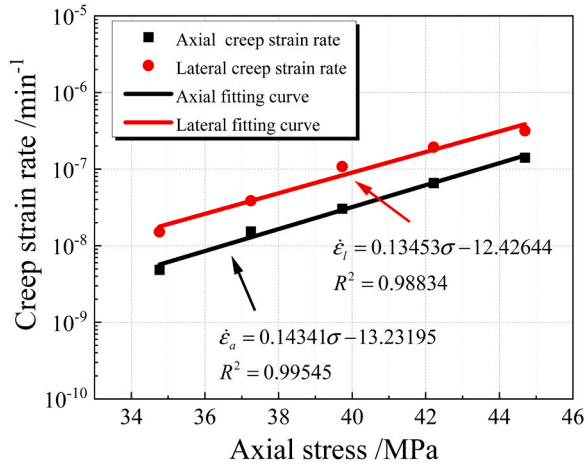

Fig. 11. Variations of axial and lateral creep strain rates against axial stress.

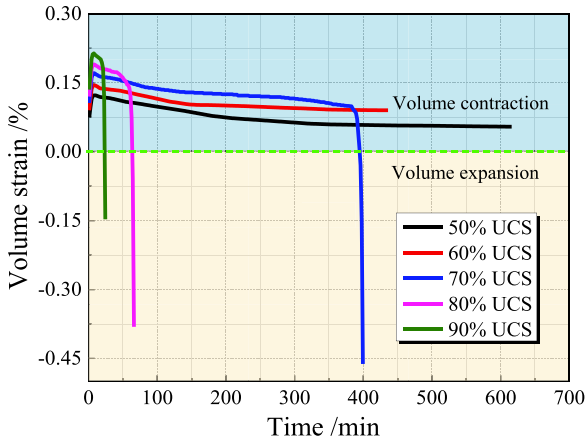

Fig. 12. Volumetric strain as a function of time for simulations performed at different stress levels (50 %, 60 %, 70 %, 80 %, and 90 % of the UCS).

in the creep strain rate (Fig. 11). Large increases in creep strain rate for small increases in differential stress have previously been observed in brittle creep experiments performed in the laboratory [2], adding confidence to our modeling approach.

Fig. 12 illustrates the volumetric strain versus time curves of rocks at various stress levels (50 %, 60 %, 70 %, 80 %, and 90 % of the UCS). Fig. 12 clearly reveals that at lower stress levels (especially the stress levels of 50 % and 60 % of the UCS), the rock samples first undergo compression and then expansion during the creep stage associated with the deceleration of the creep strain rate. However, due to the greater extent of axial compressive deformation compared to lateral expansion deformation, the overall volume of the specimen decreases. At higher stress levels (e.g., at 70 %, 80 %, and 90 % of the UCS), the volume of the specimen at the start of the simulation decreases due to the greater extent of axial compressive deformation compared to lateral expansion deformation. As the strain rate slows down during decelerating creep, the lateral creep rate exceeds the axial creep rate (the lateral creep strain rate is consistently higher than the axial creep strain rate in Fig. 11), resulting in lateral expansion deformation and a gradual reduction in the trend of volume contraction. During the accelerating creep stage, there is a significant increase in the number of fractures occurring in the particle contacts. This results in a lateral expansion that far exceeds the axial compressive deformation. Consequently, the specimen undergoes a rapid transition from a volumetric contraction to a volumetric expansion, causing a sharp increase in the volume of the rock specimen and, as a result, macroscopic instability and failure. This phenomenon is clearly

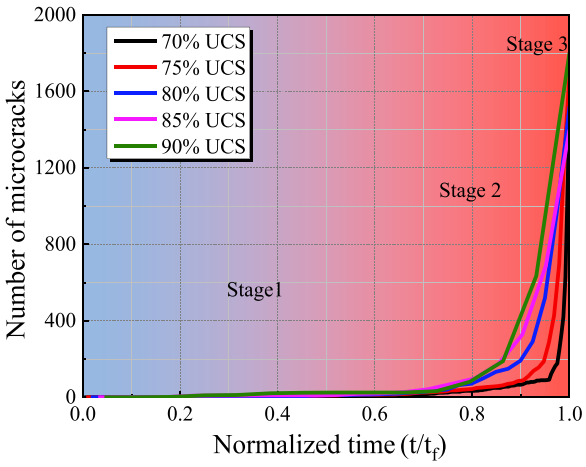

Fig. 13. Variation of the number of microcracks with normalized time for uniaxial creep simulations performed at different stress levels.

indicated by the large and sudden change observed in the volume strain curves (Fig. 12), also observed during laboratory creep experiments [6].

4.1.2. *Microcracking at different levels of loading*

To gain deeper insights into microcracking in rocks during time-dependent deformation and failure, additional uniaxial creep simulations were run at stress levels corresponding to 75 % and 85 % of the UCS. At stress levels of 50 % and 60 % of the UCS, the contact stresses between particles within the rock were minimal, falling below the stress threshold required for significant microcracking and strain accumulation. Consequently, additional simulations at stress levels of 75 % and 85 % of the UCS was vital to achieving a more comprehensive understanding of microcrack propagation during creep-induced failure in rocks.

Due to significant variations in the time-to-failure at different stress levels during creep on rocks (e.g., see Fig. 10), it was necessary to normalize the creep time using t/t_f to investigate the number of microcracks that formed during the creep process at different stress levels (as illustrated in Fig. 13). In Fig. 13, t_f represents the time-to-failure, and t denotes the creep damage time. Based on Fig. 13, under the conditions of single-stage loading creep, the number of microcracks undergoes a three-stage pattern. The initial stage of microcracking (Stage 1; Fig. 13): During this stage, the number of microcracking is essentially negligible, and as the stress level increases, the duration of this stage gradually decreases. Microscopically, the number of contacts within the model that reach or exceed the stress threshold gradually increases as the stress level increases, leading to an escalation in the damage rate of the model. The stage of stable microcrack growth (Stage 2; Fig. 13): In this stage, the number of microcracking exhibits approximately linear growth, and the slope of this stage increases with higher stress levels. Microscopically, as the stress level increases, the internal damage within the model gradually increases, intensifying the fracture process and accelerating the rate of microcrack growth. The stage of rapid microcrack growth (Stage 3; Fig. 13): During this stage, the number of microcracking experiences sharp growth. Microscopically, prior to this stage, a certain number of microcracks have already formed within the model, altering its microstructure and reducing its load-carrying capacity. As a result, the number of microcracking rapidly increases, leading to instability and the failure of the model.

Fig. 14 illustrates the variation in the number of tensile and shear cracks (and the total number of cracks) over time during single-stage creep loading for different stress levels. It is clearly seen from Fig. 14 that tensile microcracks dominate the entire creep process for all stress levels. Initially, tensile cracks form, causing a weakening of the internal structure of the numerical specimen, leading to the generation of shear

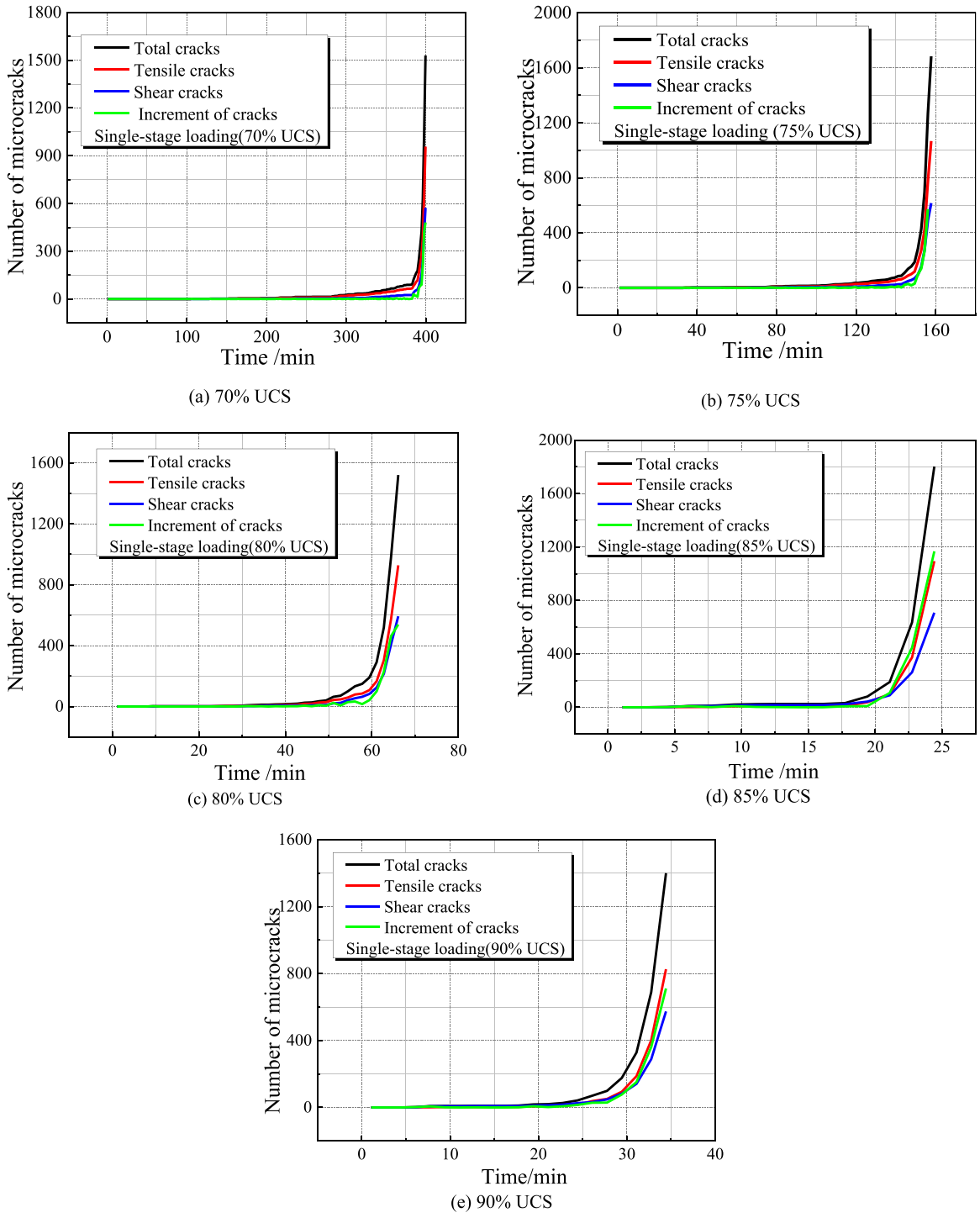

Fig. 14. Number of microcracks (tensile, shear, and total) as a function of time for creep simulations performed at different stress levels.

microcracks. During the stage of stable microcrack growth, both tensile and shear microcracks within the model exhibit an increasing trend, leading to further deterioration of the internal load-bearing structure within the model. In the stage of rapid microcrack growth, the internal load-carrying capacity in the model becomes significantly diminished due to the prior accumulation of a substantial number of microcracks. The number of microcracking experiences sharp growth during this stage, resulting in a rapid increase in strain and the subsequent failure of the model (Fig. 14).

The spatial distribution of microcracks during the creep process plays a crucial role in determining the creep failure mode of rocks. Therefore, the spatial location information of microcracking during the creep simulations are recorded in the study. As depicted in Fig. 15, for the single-stage creep loading simulations, the overall pattern of microcrack distribution upon macroscopic failure remains relatively consistent between the different stress levels. However, at higher stress levels, the spatial microcracking within the model is more dispersed (e.g., Fig. 15(e)). In addition to the significant number of microcracks

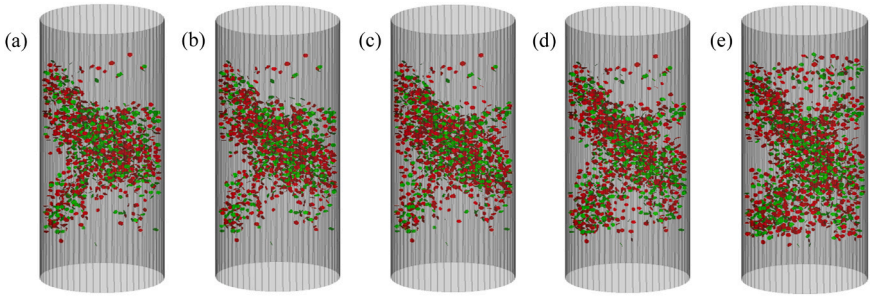

Fig. 15. The spatial distribution of microcracks during creep at different stress levels (from left to right: 70 %, 75 %, 80 %, 85 %, and 90 % of the UCS, respectively). Red color represents tensile microcracks, and green color represents shear microcracks.

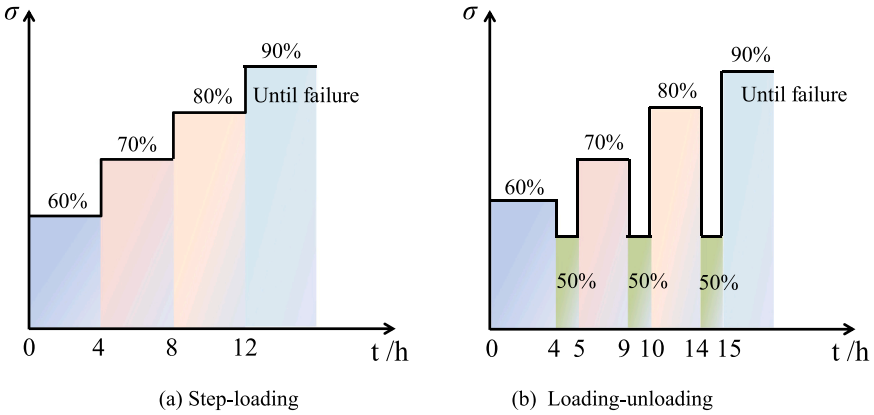

Fig. 16. Stress paths employed for the (a) multistage step-loading simulations and the (b) multistage loading-unloading simulations.

generated near the macroscopic fracture zone, a considerable quantity of microcracks also forms outside the macroscopic failure zone at high stress-levels (e.g., Fig. 15(e)). This type of microcracking behavior at high stress levels exacerbates the failure of the specimen.

4.2. Multistage creep tests

The multistage step-loading, and multistage loading-unloading creep test simulations were performed using servo control applied to the upper and lower loading plates, enabling the maintenance of a constant axial stress during both loading and unloading. Two sets of stress paths were employed for the multistage loading simulations, presented in Fig. 16. The procedure for the multistage step-loading simulations consisted of incrementally increasing the stress level from 60 % to 90 % in a stepwise manner, with each stage being maintained for a duration of 4 hours (Fig. 16(a)). In the multistage loading-unloading simulations, following each loading stage, the stress was unloaded to 50 % and held for 1 hour before applying the next level of load (Fig. 16(b)). This approach was adopted to investigate the deformation behavior of rocks under various stress paths during creep.

4.2.1. Creep under multistage loading

According to the stress loading scheme described above (Fig. 16), the corresponding axial and lateral strain versus time curves are presented in Fig. 17. Under multistage step-loading conditions (Fig. 16(a)), both axial and lateral strains exhibit typical time-dependent creep deformation (Fig. 17(a)). In the initial stages of each stress increment, the specimen undergoes significant elastic deformation (Fig. 17(a)). Subsequently, both axial and lateral strains evolve as a function of time under constant stress. At lower stress levels, the axial strain increases slowly and eventually stabilize after entering the creep stage. However, as the stress level increases, the axial and lateral strain of the specimen rapidly increases, leading to eventual macroscopic failure under high-stress conditions (Fig. 17(a)).

From a microscopic perspective, at lower stress levels, the number of microcracking within the specimen remains stable as the internal contact stresses reach the stress corrosion threshold. The axial and lateral strains remain relatively unchanged (as observed in Fig. 17(a), at stress levels of 60 %, 70 %, and 80 % of the UCS). In the later stages of creep failure, the mechanical properties of the particle contacts in the numerical specimen further deteriorate, rendering a significant number of internal contacts unable to sustain the loads. Consequently, there is a rapid increase in macroscopic strain within the model, ultimately resulting in macroscopic failure (as observed in Fig. 17(a), at a stress level corresponding to 90 % of the UCS).

Under the conditions of multistage loading-unloading (Fig. 16(b)), the creep behavior of the model exhibits a similar trend to that observed in the multistage step-loading scenario (compare Fig. 17(a) with Fig. 17 (b)). This is demonstrated in Fig. 18, which compares the strain-time curves from Fig. 17 (after removing the unloading phase in the multistage loading-unloading simulation). It can be observed that, despite the previous indication in Section 4.1.1 that the axial strain of the model remains nearly unchanged and the internal damage is minimal at a stress level corresponding to 50 % of the UCS, the implementation of multistage loading still has a detrimental effect on the model, even when it is unloaded to the same 50 % stress level. This effect becomes evident in the difference in time-to-failure between the multistage step-loading simulation and the multistage loading-unloading simulation (Fig. 18), serving as a direct reflection of the impact of multistage loading on the behavior of the model.

4.2.2. Microcracking under multistage loading

The relationship between the number of microcracks (tensile, shear, and total) in the model versus time during multistage step-loading and multistage loading-unloading is shown in Fig. 19(a) and Fig. 19(b), respectively. At lower stress levels (e.g., 60 % and 70 % of the UCS), no

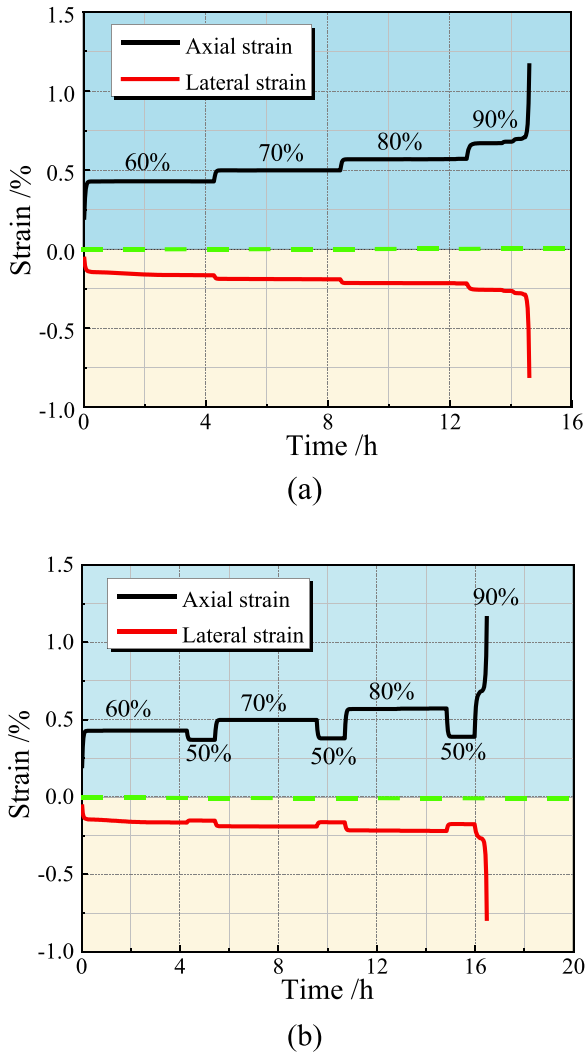

Fig. 17. Axial and lateral strain versus time variations for (a) a multistage step-loading simulation and the (b) a multistage loading-unloading simulation.

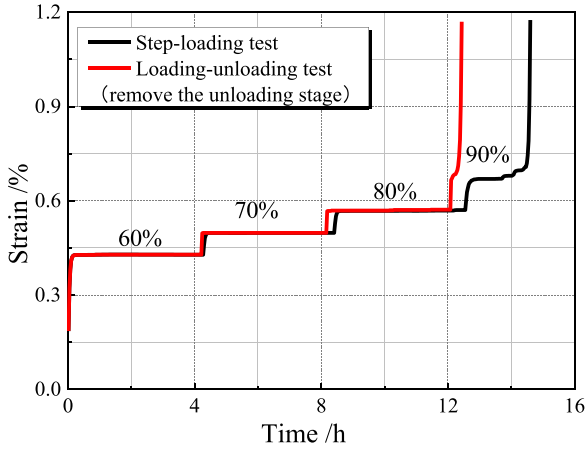

Fig. 18. Comparison between the evolution of strain against time for the step-loading and loading-unloading test simulations.

microcracks are observed within the model. However, at higher stress levels (e.g., 80 % of the UCS), both tensile and shear microcracks begin to develop within the model, without a clear sequence of initiation between them. When the model eventually fails, the number of tensile cracks still exceeds the number of shear microcracks. Hence, in the context of multistage loading (step-loading and loading-unloading), tensile microcracks play a dominant role in the creep failure process of rocks.

Under multistage step-loading conditions, microcracks generated by creep gradually form an inclined shear fracture, with the majority of microcracks concentrated in this region (Fig. 20(a)). The development of these microcracks weakens the cohesion in the direction of the fracture, resulting in the formation of a macroscopic shear fracture under the influence of external loads. This phenomenon bears a strong resemblance to the failure mode observed in uniaxial compression, where the initiation of tensile cracks leads to the formation of a shear fracture.

Although the numerical specimen subjected to multistage loading-unloading also formed an inclined shear fracture (Fig. 20(b)), the failure pattern appears more fragmented compared to that observed during multistage step-loading (Fig. 20(a)). Hence, further investigation is warranted to explore the creep failure behavior of rocks under complex stress conditions in practical engineering scenarios.

4.3. *Confining pressure dependence*

Studying the influence of confining pressure on rock creep is primarily achieved in the model by applying servo control to the upper and lower loading plates and the side walls, thereby achieving constant axial stress and lateral stress loading. Two schemes of creep simulations were conducted to study the influence of confining pressure. Each scheme had two different confining pressures: 5 MPa and 10 MPa. The specific loading configurations were as follows:

Scheme A: Confining pressure of 5 MPa, axial stress levels of 40, 45, 50, 55, and 60 MPa.

Scheme B: Confining pressure of 10 MPa, axial stress levels of 45, 50, 55, 60, and 65 MPa.

In these simulations, the confining pressure was controlled to maintain a constant value while the axial stress was varied to investigate the impact of confining pressure on rock creep behavior.

4.3.1. *Creep deformation characteristics under confining pressure*

Fig. 21 presents the results of the creep simulations conducted under confining pressures of 5 MPa (Fig. 21(a)) and 10 MPa (Fig. 21(b)). Fig. 21 shows that the deformation behavior of the model during creep is qualitatively similar to the results obtained from the uniaxial creep simulations (shown in Fig. 10). Specifically, as the axial stress increases, the time-to-failure decreases (Fig. 21).

In this study, the results of creep simulations under axial stresses of 45 and 60 MPa were compared to investigate the impact of different confining pressures on rock creep under the same axial stress. This comparison is presented in Fig. 22, which demonstrates that higher confining pressures can effectively reduce both axial and lateral strains in rocks when subjected to the same axial stress. For example, the axial strain under a confining pressure of 10 MPa is smaller than the axial strain under a confining pressure of 5 MPa (Fig. 22(a)). A similar trend is observed for lateral strain (Fig. 22(b)). This phenomenon can be attributed to the fact that high confining pressure limits the lateral deformation of the rock. According to Poisson's effect, under higher confining pressures (e.g., 10 MPa), the rock experiences additional elongation in the axial direction, counterbalancing the compressive effect of the axial stress. Consequently, under higher confining pressures, the axial strain in the rock is reduced compared to that under lower confining pressures. Fig. 22 also shows that the time-to-failure is greatly increased when the confining pressure is increased from 5 to 10 MPa. The results of our numerical simulations are in line with those from laboratory brittle creep experiments, which also showed that, for a given differential stress, the creep strain rate is higher and the time-to-failure is shorter at lower effective pressures (e.g., Heap et al. [6]).

Fig. 23 shows the axial and lateral creep strain rate as a function of

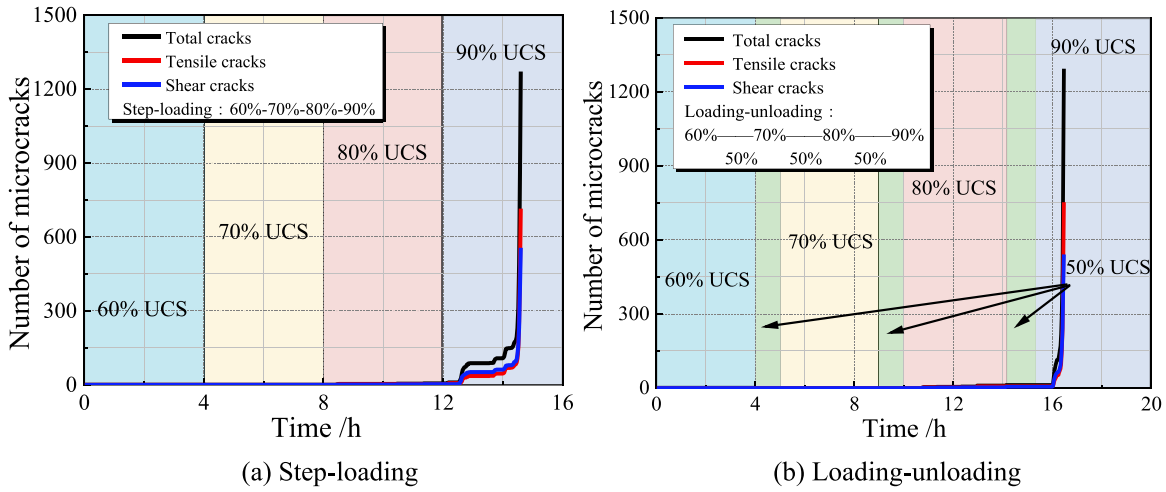

Fig. 19. The number of microcracks formed during (a) a multistage step-loading simulation and (b) a multistage loading and unloading simulation.

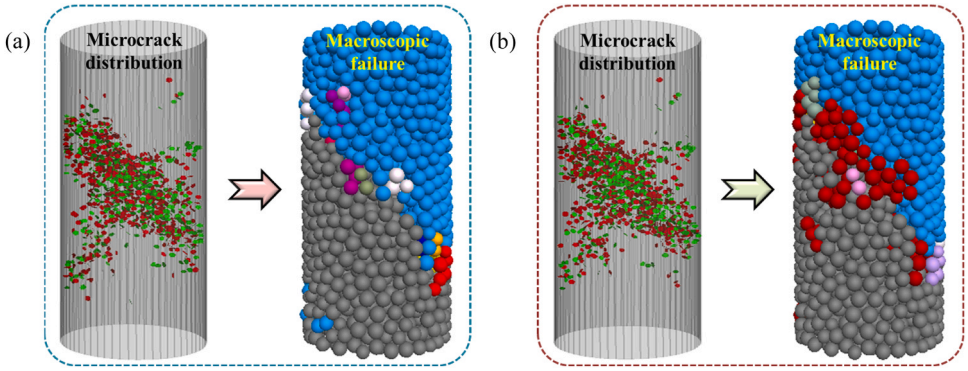

Fig. 20. The distribution of microcracks and the macroscopic failure of specimens subjected to (a) a multistage step-loading and (b) multistage loading-unloading.

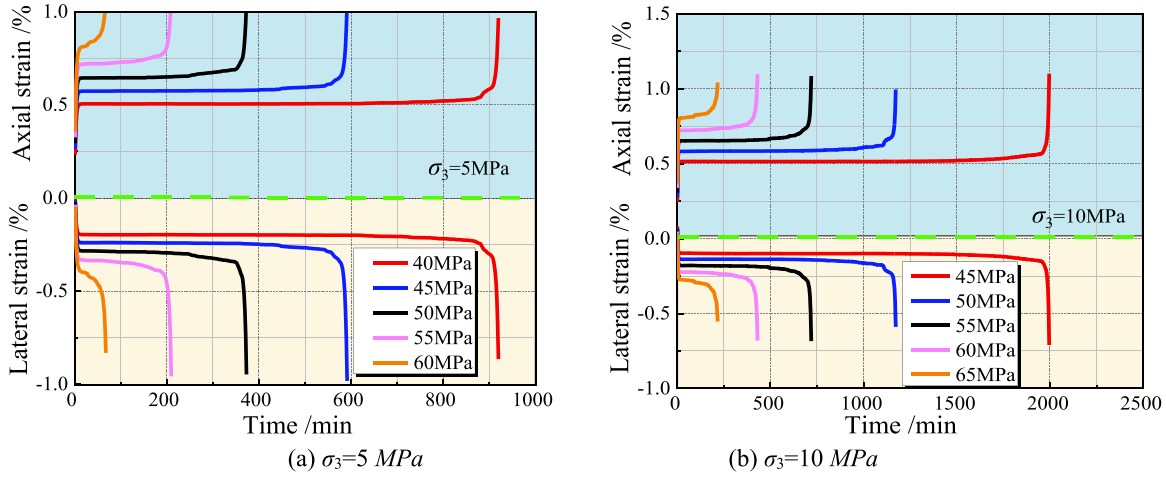

Fig. 21. Axial and lateral creep curves for simulations performed under different confining pressures of (a) 5 MPa and (b) 10 MPa.

axial stress for simulations performed at confining pressures of 5 and 10 MPa. Fig. 23 shows that, at both confining pressures of 5 and 10 MPa, the creep strain rate of the specimens increases as the differential axial stress increases (as also found for the uniaxial simulations; see Fig. 11). Fig. 23 also shows that the increase in creep strain rate for a given increase in axial stress is the same for the simulations performed at 5 and 10 MPa. However, there are notable distinctions in the creep behavior between the confining pressure of 5 and 10 MPa. Firstly, at a given stress level, the creep strain rate is higher when the confining pressure is 5 MPa compared to 10 MPa, as depicted in Fig. 23. Secondly, under a confining pressure of 10 MPa, the lateral creep strain rate of the rock is nearly equal to the axial creep strain rate. Conversely, under a confining pressure of 5 MPa, the lateral creep strain rate surpasses the axial creep strain rate (we also note that the lateral creep strain rate exceeds the axial creep strain rate in our uniaxial simulations, as shown in Fig. 11). Based on these observations, it can be concluded that confining pressure

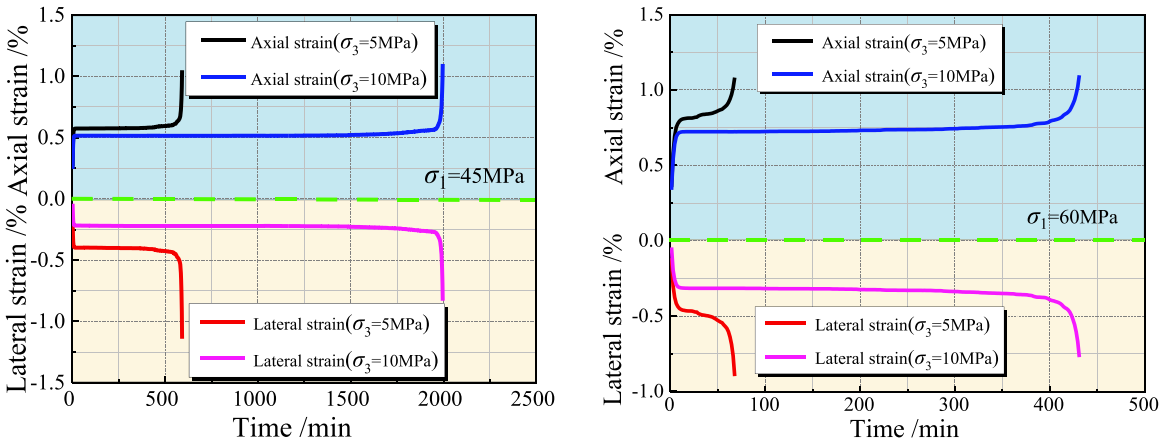

(a) σ_1=45*MPa* (b) σ_1=60*MPa*

Fig. 22. The influence of confining pressure on creep behavior under the same axial stress of (a) 45 MPa and (b) 60 MPa.

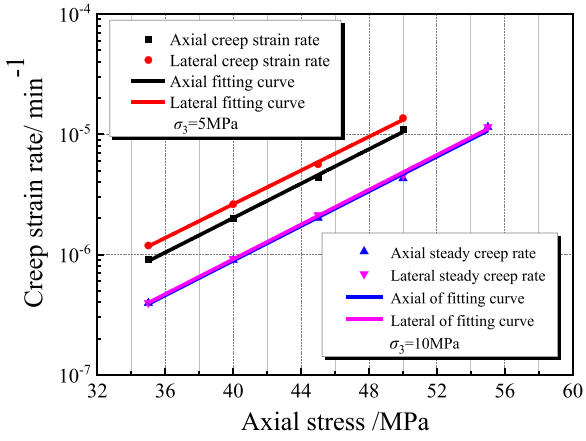

Fig. 23. Relationship curve between creep strain rate and axial stress under different confining pressures (5 and 10 MPa).

has a restrictive effect on rock creep. In other words, higher confining pressures can diminish the creep rate of rocks, thereby enhancing their mechanical performance when subjected to long-term sustained loading. Therefore, in practical rock engineering, providing active support can effectively enhance the mechanical performance of rock masses.

4.3.2. Creep microcrack characteristics under confining pressure

In creep simulations performed under confining pressure, we notice that the presence of microcracks is influenced not only by the magnitude of axial stress, but also by the magnitude of the confining pressure (Fig. 24). Fig. 24(a) shows that the total number of microcracks formed following creep failure decreases linearly with increasing axial stress, both at confining pressures of 5 and 10 MPa. Additionally, Fig. 24(a) also demonstrates that, for a given axial stress, the total number of microcracks formed following creep failure decreases as confining pressure is increased from 5 to 10 MPa. This finding is consistent with the earlier conclusion that confining pressure can enhance the mechanical performance of rocks.

Fig. 24(b) and (c) show the number of tensile and shear microcracks for simulations performed at various axial stresses under confining pressures of 5 and 10 MPa, respectively. These figures reveal that as the axial stress increases, the number of tensile cracks gradually decreases, and their proportion relative to the total number of microcracks decreases, indicating a reduced role in failure. Meanwhile, the proportion of shear cracks gradually increases as the axial stress increases. Comparing the results at a confining pressure of 5 MPa (Fig. 24(b)) with 10 MPa (Fig. 24(c)), we can see that, at high stresses, the relative number of shear to tensile cracks increases as confining pressure is increased from 5 to 10 MPa. Therefore, these findings demonstrate that increasing the confining pressure restricts the formation of tensile microcracks.

Fig. 25 presents the spatial distribution of microcracks at different axial stresses (40, 45, 50, 55, and 60 MPa) under confining pressures of 5 and 10 MPa. It can be observed from Fig. 25 shows that, regardless of the axial stresses and confining pressures applied, the occurrence of macroscopic failure is attributed to the development of an inclined shear fracture. In other words, increasing the confining pressure from 5 to 10 MPa does not change the mode of creep failure. Furthermore, it is evident that, for a given confining pressure, macroscopic failure is more localized at higher stresses (Fig. 25). However, when considering a specific axial stress, there is minimal variation in the distribution of microcracks as the confining pressure increases from 5 to 10 MPa (Fig. 10). Therefore, it can be concluded that the influence of confining pressure on the distribution of microcracks within the model is comparatively less significant than the influence of axial stress.

It is noted that the number of particles used in a simulation can have a significant impact on the accuracy and reliability of the results in the DEM modelling. A larger number of particles improves the statistical significance of the results, reducing random fluctuations and providing a more representative simulation as well as capture fine details of the rock behavior such as local stress distributions and particle interactions. However, increasing the number of particles increases computational resources and simulation time, balancing accuracy with computational efficiency. Sensitivity analyses help determine the optimal number of particles, with validation against experimental data aiding in assessing the model's accuracy. Thus, the number of particles in a DEM simulation plays a critical role in determining the accuracy, reliability, and computational efficiency of the results. Careful consideration of factors such as statistical significance, spatial resolution, computational cost, and system size effects is essential in determining an appropriate number of particles to achieve meaningful and reliable simulation outcomes [48,65,66].

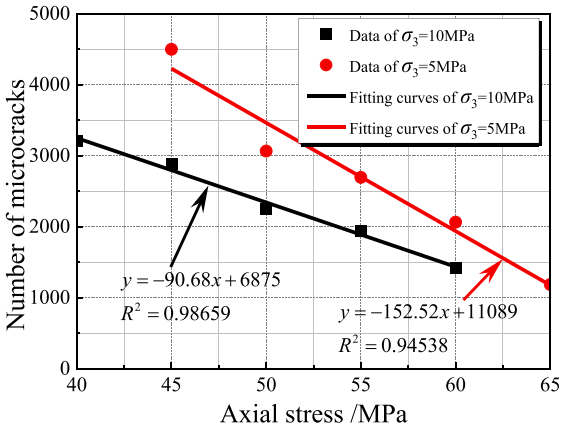

(a) Total microcrack number

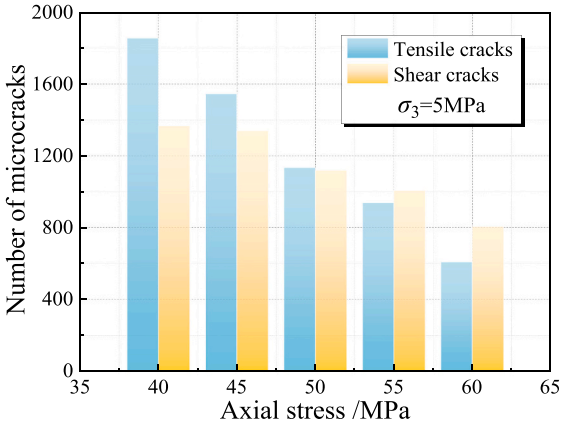

(b) Number of micro-cracks when σ_3 =5 MPa

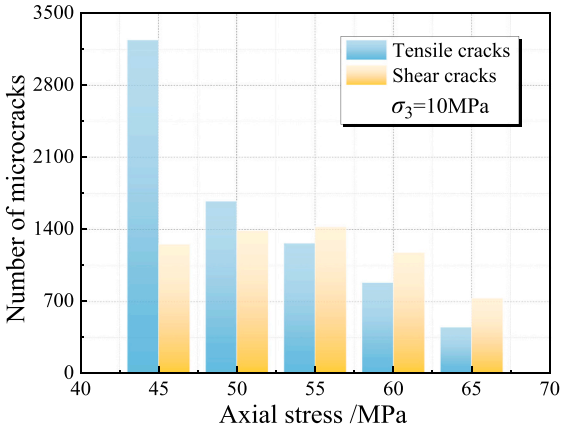

(c) Number of micro-cracks when σ_3=10 *MPa*

Fig. 24. The variations of the number of microcracks against axial stress for different confining pressures (5 and 10 MPa).

5. Conclusions

In this study, numerical simulations were conducted to investigate the creep behaviour of rocks under various loading conditions, including single-stage creep loading, multistage creep loading, and under confinement, at various stress levels. The objective was to analyze the effects of different loading conditions on rock creep. The PSC model was integrated into the three-dimensional PFC3D to establish a time-dependent deformation damage and fracture process model of rock based on the discrete element method. This model was used to conduct uniaxial compression and uniaxial creep tests on rocks, and the obtained results were compared with and validated against laboratory experiments. Our findings demonstrate that the model effectively captures the creep characteristics of rocks and accurately simulates the decelerating and accelerating creep behavior observed in laboratory experiments.

Under single-stage creep loading conditions, the occurrence of accelerated creep in rocks is closely influenced by factors such as the magnitude of the applied stress and the mechanical properties of the rocks. When the applied stress is significantly below the long-term strength of the rock, minimal or no damage occurs within the rock, and the axial strain does not exhibit an accelerating stage. However, when the applied stress surpasses the long-term strength, the axial strain of the rock enters an accelerating stage, leading to instability and macroscopic failure of the specimen. The lateral creep strain and volumetric creep strain curves display similar trends. The simulation results of the single-stage creep loading of rocks indicate that the propagation of microcracks can be classified into three stages: an initial stage, a stable growth stage, and a rapid increase and failure stage. During the creep damage and instability process of rocks, tensile cracks are the predominant type, with shear cracks assuming a secondary role, ultimately resulting in the formation of a macroscopic shear fracture. Under multistage loading conditions, as stress levels increase, the axial and lateral strain of the specimen rapidly increases, microcracks experience rapid growth during the late stages of the simulation when the stress level is high, leading to a volumetric expansion of the rock specimen and eventual macroscopic failure.

The creep behavior of the model exhibits a similar trend in the multi-stage step-loading and multi-stage loading-unloading. The difference in time-to-failure between the multistage step-loading simulation and the multistage loading-unloading simulation could serve as a direct reflection of the impact of multistage loading on the behavior of the model. Tensile microcracks play a dominant role in the creep failure process of rocks in the context of multistage loading (step-loading and loading-unloading). The numerical specimen subjected to multistage step-loading and loading-unloading both form an inclined shear fracture, the failure pattern of specimen under loading-unloading appears more fragmented compared to that observed during multistage step-loading.

Creep simulations performed under different confining pressures show that creep behaviour and the variation of microcracks in rocks is influenced not only by the magnitude of the confining pressure, but also by the magnitude of the axial stress. Under identical axial stress conditions, increasing the confining pressure imposes a limiting effect on the creep strain rate and can effectively reduce both axial and lateral strains in rocks, thus enhancing the mechanical performance of rocks. Conversely, under the same confining pressure conditions, increasing the axial stress increases the creep strain rate, but reduces the number of

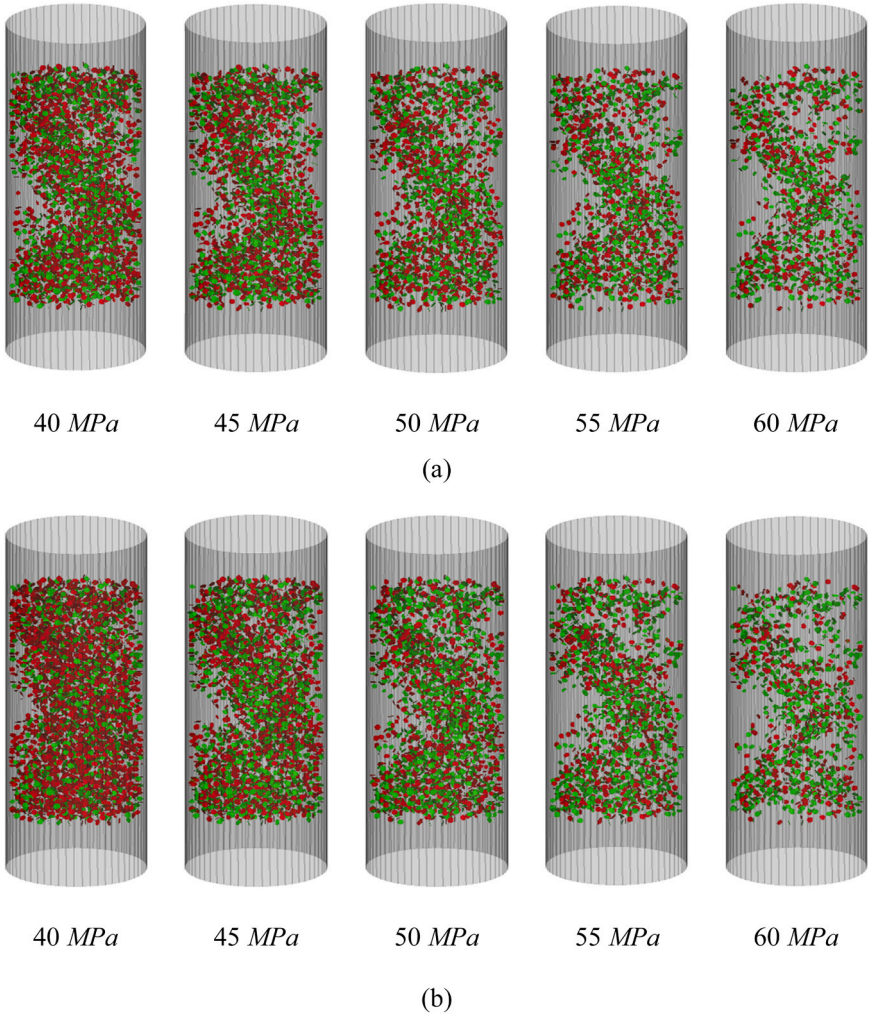

Fig. 25. The distribution of microcracks following creep failure under confining pressures σ_3 of 5 and 10 MPa.

microcracks in the model at the point of failure. Furthermore, the influence of confining pressure on the distribution of microcracks in the model is less than the influence of axial stress. These findings reveal the creep mechanism from a microscopic perspective and important implications can be directed to the long-term stability of rock engineering projects such as underground gas storage, underground tunnel supports and compressed air energy storage.

CRediT authorship contribution statement

Tao Xu: Writing – review & editing, Methodology, Investigation, Funding acquisition, Formal analysis, Conceptualization. **Zhen Heng:** Writing – original draft, Investigation, Data curation. **Ben Liu:** Writing – original draft, Formal analysis, Data curation. **Michael J. Heap:** Writing – review & editing, Methodology. **P.L.P. Wasantha:** Writing – review & editing, Investigation. **Zhiguo Li:** Visualization.

Declaration of Competing Interest

I have read and understood the policy of *Deep Resources Engineering* on declaration of interests and there are no conflicts to declare.

Acknowledgements

This work was supported by the National Natural Science Foundation of China (grant numbers 42172312, 52211540395). M. Heap acknowledges support from the Institut Universitaire de France (IUF).

References

[1] W. Blum, P. Eisenlohr, F.J.M. Breutinger, M.T. A, Underst. creep—a Rev. 33 (2002) 291–303.
[2] N. Brantut, M.J. Heap, P.G. Meredith, P. Baud, Time-dependent cracking and brittle creep in crustal rocks: a review, J. Struct. Geol. 52 (2013) 17–43.
[3] N. Brantut, M.J. Heap, P. Baud, P.G. Meredith, Rate- and strain-dependent brittle deformation of rocks, J. Geophys Res-Solid Earth 119 (2014) 1818–1836.
[4] R.L. Kranz, Crack growth and development during creep of Barre granite, Int. J. Rock. Mech. Min. Sci. Geomech. Abstr. 16 (1979) 23–25.
[5] D. Lockner, Room temperature creep in saturated granite, J. Geophys. Res.: Solid Earth 98 (1993) 475–487.
[6] M.J. Heap, P. Baud, P.G. Meredith, A.F. Bell, I.G. Main, Time-dependent brittle creep in Darley Dale sandstone, J. Geophys Res-Solid Earth 114 (2009) 22.
[7] C.F. Chen, T. Xu, M.J. Heap, P. Baud, Influence of unloading and loading stress cycles on the creep behavior of Darley Dale Sandstone, Int. J. Rock. Mech. Min. Sci. 112 (2018) 55–63.
[8] M.J. Heap, P. Baud, P.G. Meredith, Influence of temperature on brittle creep in sandstones, Geophys Res. Lett. 36 (2009) 6.
[9] Y.C. Xue, T. Xu, M.J. Heap, P.G. Meredith, T.M. Mitchell, P.L.P. Wasantha, Time-dependent cracking and brittle creep in macrofractured sandstone, Int. J. Rock. Mech. Min. Sci. 162 (2023).
[10] N. Brantut, M.J. Heap, P. Baud, P.G. Meredith, Mechanisms of time-dependent deformation in porous limestone, J. Geophys. Res.-Solid Earth 119 (2014) 5444–5463.
[11] A. Nicolas, J. Fortin, J.B. Regnet, B.A. Verberne, O. Plumper, A. Dimanov, et al., Brittle and semibrittle creep of Tavel limestone deformed at room temperature, J. Geophys Res. B: Solid Earth 122 (2017) 4436–4459.
[12] M.J. Heap, P. Baud, P.G. Meredith, S. Vinciguerra, A.F. Bell, I.G. Main, Brittle creep in basalt and its application to time-dependent volcano deformation, Earth Planet Sc. Lett. 307 (2011) 71–82.

[13] B.K. Atkinson, Subcritical crack growth in geological materials, J. Geophys. Res.: Solid Earth 89 (1984) 4077–4114.
[14] Y. Xue, T. Xu, M.J. Heap, W. Zhu, P.G. Ranjith, Z. Li, Effect of pH on primary and secondary crack propagation in sandstone under constant stress (creep) loading, Constr. Build. Mater. 421 (2024) 135727.
[15] Z. Li, T. Xu, L. Zhao, Y. Liu, Y. Xu, M.J. Heap, et al., Enhancing stability analysis of open-pit slopes via integrated 3D numerical modeling and data monitoring, Eng. Fail. Anal. 163 (2024) 108495.
[16] X.-y Yu, T. Xu, M.J. Heap, Z. Heng, P.G. Ranjith, B. Su, et al., Time-dependent virtual crack model of rock with application to slope stability, Eng. Anal. Bound. Elem. 154 (2023) 172–185.
[17] T.-F. Fu, T. Xu, P.L.P. Wasantha, T.-H. Yang, Y. Nara, Z. Heng, Time-dependent deformation and fracture evolution around underground excavations, Geomat., Nat. Hazards Risk 11 (2020) 2615–2633.
[18] C.C. Li, Field observations and interpretation of extensional fracture in hard rock surrounding deep underground openings, Deep Resour. Eng. 1 (2024) 100006.
[19] J.-F. Shao, Z. Yu, Z. Liu, M.-N. Vu, G. Armand, Numerical analysis of thermo-hydromechanical process related to deep geological radioactive repository, Deep Resour. Eng. 1 (2024) 100001.
[20] W. Wang, H.X. Liu, Q.Z. Zhu, J.F. Shao, A micromechanics-based creep damage model for brittle rocks, Eur. J. Environ. Civ. Eng. 19 (2015) S1–S14.
[21] L.F. Zhu, L.Q. Wang, L.B. Zheng, N. Xie, C.S. Wang, Z.H. Sun, et al., Shear creep characteristics and creep constitutive model of bolted rock joints, Eng. Geol. 327 (2023) 24.
[22] B. Xu, T. Xu, M.J. Heap, A.R.L. Kushnir, B.-Y. Su, X.-C. Lan, An adaptive phase field approach to 3D internal crack growth in rocks, Comput. Geotech. 173 (2024) 106551.
[23] J.W. Ma, Z.Y. Wang, J.P. Wu. Probability Distribution Analysis of Rock Salt Creep Parameters Based On Comprehensive Optimal Acceptance Criteria. 12th International Conference on Fracture and Damage Mechanics (FDM 2013). Trans Tech Publications Ltd, Sardinia, ITALY, 2013. pp. 561-564.
[24] R.B. Hou, K. Zhang, J. Tao, X.R. Xue, Y.L. Chen, A nonlinear creep damage coupled model for rock considering the effect of initial damage, Rock. Mech. Rock. Eng. 52 (2019) 1275–1285.
[25] Y.R. Liu, W.Q. Wa, Z. He, S. Lyv, Q. Yang, Nonlinear creep damage model considering effect of pore pressure and analysis of long-term stability of rock structure, Int. J. Damage Mech. 29 (2020) 144–165.
[26] N. Brantut, P. Baud, M.J. Heap, P.G. Meredith, Micromechanics of brittle creep in rocks, J. Geophys. Res.-Solid Earth 117 (2012).
[27] M.F. Ashby, C.G. Sammis, The damage mechanics of brittle solids in compression, Pure Appl. Geophys 133 (1990) 489–521.
[28] N. N. Danesh, Z.W. Chen, L.D. Connell, M.S. Kizil, Z.J. Pan, S.M. Aminossadati, Characterisation of creep in coal and its impact on permeability: An experimental study, Int. J. Coal Geol. 173 (2017) 200–211.
[29] Y.S. Li, C.C. Xia, Time-dependent tests on intact rocks in uniaxial compression, Int. J. Rock. Mech. Min. Sci. 37 (2000) 467–475.
[30] D.P. Singh, A study of creep of rocks, Int. J. Rock. Mech. Min. Sci. 12 (1975) 271–276.
[31] G.N. Boukharov, M.W. Chanda, N.G. Boukharov, The three processes of brittle crystalline rock creep, Int. J. Rock. Mech. Min. Sci. Geomech. Abstr. 32 (1995) 325–335.
[32] S.W. Hao, C. Liu, Y.C. Wang, F.Q. Chang, Scaling law of average failure rate and steady-state rate in rocks, Pure Appl. Geophys. 174 (2017) 2199–2215.
[33] D. Cruden, The static fatigue of brittle rock under uniaxial compression, Int J. Rock. Mech. Min. Sci. 11 (1974) 67–73.
[34] B. Voight, A method for prediction of volcanic eruption, Nature 332 (1988) 125–130.
[35] B. Voight, A relation to describe rate-dependent material failure, Science 243 (1989) 200–203.
[36] D.A. Lockner, A generalized law for brittle deformation of Westerly granite, J. Geophys Res B: Solid Earth 103 (1998) 5107–5123.
[37] C.H. Scholz, Mechanism of creep in brittle rock, J. Geophys. Res. 73 (1968) 3295–3302.
[38] D. Lockner, Room temperature creep in saturated granite, J. Geophys. Res. 98 (1993) 475–487.
[39] N. Barton, E. Quadros, Anisotropy is everywhere, to see, to measure, and to model, Rock. Mech. Rock. Eng. 48 (2015) 1323–1339.
[40] C. Saroglou, S.W. Qi, S. Guo, F. Wu, ARMR, a new classification system for the rating of anisotropic rock masses, B Eng. Geol. Environ. 78 (2019) 3611–3626.
[41] W.B. Guo, B. Hu, J.L. Cheng, B.F. Wang, Modeling time-dependent behavior of hard sandstone using the DEM method, Geomech. Eng. 20 (2020) 517–525.
[42] N. Bahrani, P.K. Kaiser, B. Valley, Distinct element method simulation of an analogue for a highly interlocked, non-persistently jointed rockmass, Int. J. Rock. Mech. Min. Sci. 71 (2014) 117–130.
[43] W. Chen, H. Konietzky, Simulation of heterogeneity, creep, damage and lifetime for loaded brittle rocks, Tectonophysics 633 (2014) 164–175.
[44] Y. Lin, J. Ma, Z. Lai, L. Huang, M. Lei, A FDEM approach to study mechanical and fracturing responses of geo-materials with high inclusion contents using a novel reconstruction strategy, Eng. Fract. Mech. 282 (2023) 109171.
[45] P. Deng, Q. Liu, X. Huang, Y. Pan, J. Wu, FDEM numerical modeling of failure mechanisms of anisotropic rock masses around deep tunnels, Comput. Geotech. 142 (2022) 104535.
[46] P. Qiu, T. Pabst, Waste rock segregation during disposal: calibration and upscaling of discrete element simulations, Powder Technol. 412 (2022) 117981.
[47] H. Zhao, H. Jiang, H. Li, X. Zhang, M. Zhao, Numerical research on rock cutting by abrasive jet under confining pressure based on SPH-FEM method, Powder Technol. 433 (2024) 119196.
[48] G.-F. Zhao, Q. Yin, A.R. Russell, Y. Li, W. Wu, Q. Li, On the linear elastic responses of the 2D bonded discrete element model, Int. J. Numer. Anal. Methods Geomech. 43 (2019) 166–182.
[49] F. Tiedtke, H. Konietzky, F. Magri, A novel DFN-DEM approach to simulate long-term behavior of crystalline rock under effects of glacial climate conditions, Deep Resour. Eng. 1 (2024) 100002.
[50] C. Xia, Z. Liu, C.Y. Zhou, Burger's bonded model for distinct element simulation of the multi-factor full creep process of soft rock, J. Mar. Sci. Eng. 9 (2021) 19.
[51] D.O. Potyondy, Simulating stress corrosion with a bonded-particle model for rock, Int. J. Rock. Mech. Min. Sci. 44 (2007) 677–691.
[52] N. Liu, C. Zhang, W. Chu, Simulating time-dependent failure of deep marble with particle flow code Chinese, J. Rock. Mech. Eng. 30 (2011) 1986–1996.
[53] J. Sun, M. Chen, Q. Jiang, Numerical simulation of mesomechanical characteristics of creep demage evolution for Jingping marble, Rock. Soil Mech. 34 (2013) 3601–3608.
[54] Z. Yang, A.J, Y. Zhou, Parametric analysis of Burgers model and creep properties of rock with particle flow code, Rock. Soil Mech. 36 (2015) 240–248.
[55] X. Hu, K. Bian, J. Liu, B. Li, M. Chen, Discrete element simulation study on the influence of microstructure heterogeneity on the creep characteristics of granite, Chin. J. Rock. Mech. Eng. 38 (2019) 2069–2083.
[56] Y.Y. Zhang, Z.S. Shao, W. Wei, R.J. Qiao, PFC simulation of crack evolution and energy conversion during basalt failure process, J. Geophys Eng. 16 (2019) 639–651.
[57] K. Bisdom, H.M. Nick, G. Bertotti, An integrated workflow for stress and flow modelling using outcrop-derived discrete fracture networks, Comput. Geosci. 103 (2017) 21–35.
[58] B.K. Atkinson, P.G. Meredith, the theory of subcritical crack growth with applications to minerals and rocks, Fract. Mech. Rock. 4 (1987) 111–166.
[59] W. Hillig, R. Charles, Surfaces, stress-dependent surface reactions, and strength, High. Strength Mater. (1965) 682–705.
[60] S.W. Freiman, Effects of chemical environments on slow crack growth in glasses and ceramics, J. Geophys. Res.: Solid Earth 89 (1984) 4072–4076.
[61] T.-F. Fu, T. Xu, M.J. Heap, P.G. Meredith, T.M. Mitchell, Mesoscopic time-dependent behavior of rocks based on three-dimensional discrete element grain-based model, Comput. Geotech. 121 (2020) 103472.
[62] S.W. Hao, H.Y. Wang, M.F. Xia, F.J. Ke, Y.L. Bai, Relationship between strain localization and catastrophic rupture, Theor. Appl. Fract. Mech. 48 (2007) 41–49.
[63] M.S. Paterson, T.F. Wong, Experimental rock deformation: the brittle field, Springer, Berlin, 2005.
[64] T. Xu, C. Tang, J. Zhao, L. Li, M.J. Heap, Modelling the time-dependent rheological behaviour of heterogeneous brittle rocks, Geophys. J. Int. 189 (2012) 1781–1796.
[65] C.J. Coetzee, Review: Calibration of the discrete element method, Powder Technol. 310 (2017) 104–142.
[66] H. Zhao, L. Zhang, Z. Wu, A. Liu. A new discrete element model for rock-like materials, Comput. Struct. 261- 262 (2022) 106730.

Tao Xu received his PhD from Northeastern University, Shenyang, China in 2005. He is a professor and a doctoral supervisor in the School of Resources and Civil Engineering at Northeastern University, China. His research focuses on the time-dependent deformation and fracturing of brittle rocks, associated long-term stability of rock slope, and thermo-hydro-mechanical coupling process of rock mass. Tao is actively participating in professional activities, acting as an assessor of National Natural Science Foundation of China, China Scholarship Council, Australian Research Council, Cezch Science Foundation, some provincial and ministerial science and technological awards, and he has ever academically visited City University of Hong Kong, EPFL (École Polytechnique Fédérale de Lausanne) in Switzerland, Monash University in Australia, University of Melbourne in Australia, University of Strasbourg in France, University College London in UK, and TU Graz in Austria. He has authored over 100 international journal papers and co-authored three monographs.